showing expression changes with differences of at least twofold in magnitude from the untreated controls were selected, and the "presence" signal in more than 3/4 of samples in each group showing higher expression values were selected. Genes showing altered expression in common in the anti-thyroid agent-exposed groups were also selected.

Real-time RT-PCR: Quantitative real-time RT-PCR was performed to confirm the expression values obtained with microarrays using an ABI Prism 7000 Sequence Detection System (Applied Biosystems Japan, Tokyo, Japan). Genes those showing altered expression (≥2-fold, ≤0.5-fold) in common in the anti-thyroid agent-exposed groups as compared with untreated control offspring were randomly selected, irrespective of the presence or absence of statistically significant difference. As a result, the following seven genes (four up-regulated and three down-regulated) with known function were selected as targets: Tachykinin receptor 3 (*Tacr3*), Calbindin 1, Slit homolog 2 (Drosophila) and Pleomorphic adenoma gene-like 1 (*Plagl1*) as up-regulated examples, and Myelin-associated oligodendrocytic basic protein (*Mobp*), Endothelial differentiation, sphingolipid G-protein-coupled receptor, 8 and CCAAT/enhancer binding protein as down-regulated. RT was performed using first-round antisense RNAs prepared for microarray analysis. For real-time PCR analysis of the genes selected, ABI Assays-on-Demand™ TaqMan® probe and primer sets from Applied Biosystems (available at https://products.appliedbiosystems.com/ab/en/US/adirect/ab?cmd=catNavigate2&catID=601267)(n=4/group) were used. For quantification of the expression data, a standard curve method was applied. The expression values were normalized to two housekeeping genes, Glyceraldehyde 3-phosphate dehydrogenase and Hypoxanthine-guanine phosphoribosyltransferase.

Immunohistochemistry: To evaluate the immunohistochemical distribution of the molecules selected by microarray analysis, the brains of male pups obtained at PND 20 or PNW 11 were fixed in Bouin's solution at room temperature overnight. Six animals were used as untreated controls, six for 200 ppm MMI, eight for 3 ppm PTU, and nine for 12 ppm PTU on PND 20. On PNW 11, 10 animals were used as untreated controls and 10 for 200 ppm MMI, nine for 3 ppm PTU, and six for 12 ppm PTU.

Immunohistochemistry was performed on the brain tissue sections of PND 20 and PNW 11 animals with antibodies against Ephrin type A receptor 5 (EphA5; rabbit IgG, 1:50; Abcam, Cambridge, U.K.) and Tacr3 (rabbit polyclonal antibody, 1:3,000, Novus Biologicals, Inc., Littleton, CO, U.S.A.), which were incubated with the tissue sections overnight at 4°C. Antigen retrieval treatment was not performed for these antigens. Immunodetection was carried out using a VECTASTAIN® Elite ABC kit (Vector Laboratories Inc., Burlingame, CA, U.S.A.) with 3,3'-diaminobenzidine/H_2O_2 as the chromogen, as previously described [23]. The sections were then counterstained with hematoxylin and coverslipped for microscopic examination.

With regard to EphA5, *Efna5*, a gene encoding the representative ligand for this receptor molecule [5], was found to be up-regulated (≥2-fold) by microarray analysis in all of the groups exposed to anti-thyroid agents in the present study (Table 1). Because distribution of EphA5 has been confirmed in the pyramidal cells of the hippocampal CA1 region at both developmental and adult stages in mice and at adult stage in humans [3, 17], we selected this molecule to examine distribution changes in the present study. Tacr3 was also up-regulated in all of the MMI and PTU groups by microarray analysis and real-time RT-PCR in the present study (Table 1). Expression of Tacr3 in the hippocampal CA1 pyramidal neurons has also been confirmed in rats [11], and therefore, we also selected this molecule for examination in the expression changes in the present study.

Morphometry of immunolocalized cells and apoptotic cells: EphA5- or Tacr3-immunoreactive cells distributed in the pyramidal cell layer or stratum oriens of the hippocampal CA1 region were bilaterally counted and normalized to the number in the length of the CA1 region measured (Fig. 1). Tacr3-immunoreactive cells in the subgranular zone of the dentate gyrus were also bilaterally counted and normalized for the number in the length of the granular zone measured. For quantitative measurement of each immunoreactive cellular component, digital photomicrographs at 100-fold magnification were taken using a BX51 microscope (Olympus Optical Co., Ltd., Tokyo, Japan) attached to a DP70 Digital Camera System (Olympus Optical Co., Ltd.), and quantitative measurements were performed using the WinROOF image analysis software package (version 5.7, Mitani Corp., Fukui, Japan).

Statistical analysis: Numerical data of the number of immunoreactive cells were assessed using Student's *t*-test to compare the untreated controls with each of the anti-thyroid agent-exposed groups when the variance was homogenous among the groups using a test for equal variance. If a significant difference in variance was observed, Aspin-Welch's *t*-test was used instead. The data for gene expression levels from real-time RT-PCR analysis were analyzed by the Kruskal-Wallis test, followed by Bartlett's test. When statistically significant differences were indicated, Dunnett's multiple test was used for comparisons with the untreated controls. For the microarray data, statistical analysis was performed with GeneSpring® software, and the significance of gene expression changes was analyzed by Student's *t*-test or ANOVA between the untreated controls and each of the anti-thyroid agent-exposed groups.

RESULTS

Microarray analysis: Figure 2 shows the Venn diagram of genes showing altered expression in the microdissected CA1 pyramidal neurons in the exposure groups in combination or individually in each exposure group. Many genes were found to be up- or down-regulated in common in two of the three groups. The numbers of genes classified into common categories between the groups or individually in each group were similar in terms of up- and down-regulated genes. The number of genes showing up- or down-regula-

Table 1. List of representative genes showing up- or down-regulation common to 2-mercapto-1-methylimidazole (MMI), 3 and 12 ppm 6-propyl-2-thiouracil (PTU) (≥2-fold, ≤0.5-fold)

Gene function	Accession No.	Gene title	Symbol	MMI	3 ppm PTU	12 ppm PTU
Up-regulated genes (of 119 genes in total)						
Nervous system development	AI101660	Slit homolog 2 (Drosophila)	Slit2	3.04	2.62	7.08
Nervous system development	NM_024358.1	Notch gene homolog 2 (Drosophila)	Notch2	2.52	2.01	2.02
Nervous system development	AW527295	Ephrin A5	Efna5	3.12	3.46	4.31
Nervous system development	NM_053465.1	Fucosyltransferase 9	Fut9	2.13	6.75	2.11
Nervous system development	BE106256	Sparc/osteonectin, cwcv and kazal-like domains proteoglycan 1	Spock1	3.22	3.13	2.15
Calcium ion binding	X04280.1	Calbindin 1	Calb1	4.48	4.85	9.00
Calcium ion binding	BM386119	UDP-N-acetyl-alpha-D-galactosamine:polypeptide N-acetylgalactosaminyltransferase 3 (GalNAc-T3)	Galnt3	2.43	2.30	2.63
Calcium ion binding	BI279663	Desmocollin 2	Dsc2	2.82	2.04	5.62
Calcium ion binding	AI105369	Calmodulin-like 4	Calml4	3.40	2.25	5.59
Zinc ion binding	BE098686	Similar to Tnf receptor-associated factor 1	LOC687813	3.10	2.04	2.78
Zinc ion binding	BF562032	RAN binding protein 2	Ranbp2	3.49	2.67	2.78
Zinc ion binding	BF397925	ADAMTS-like 1	Adamtsl1	6.22	2.55	7.63
Zinc ion binding	BF395606	Splicing factor, arginine/serine-rich 7	Sfrs7	4.93	2.06	2.90
Apoptosis	NM_012760.1	Pleomorphic adenoma gene-like 1	Plagl1	3.10	4.28	6.86
Apoptosis	NM_057130.1	Harakiri, BCL2 interacting protein (contains only BH3 domain)	Hrk	2.63	2.73	3.18
Cell Adhesion	AA850909	Poliovirus receptor-related 2	Pvrl2	4.74	2.46	2.61
Cell Adhesion	AA819731	Hyaluronan and proteoglycan link protein 4	Hapln4	4.13	6.67	3.46
Cell Adhesion	BI287851	Collagen, type VI, alpha 2	Col6a2	3.45	2.19	5.12
Ion channel activity	AA851939	FXYD domain-containing ion transport regulator 6	Fxyd6	4.73	2.61	7.85
Other	NM_017053.1	Tachykinin receptor 3	Tacr3	7.32	6.19	12.49
Down-regulated genes (of 97 genes in total)						
Nervous system development	NM_031018.1	Activating transcription factor 2	Atf2	0.41	0.36	0.36
Neuron migration	BF390065	Roundabout homolog 3 (Drosophila)	Robo3	0.06	0.31	0.04
Neuron differentiation	AF115249.1	Endothelial differentiation, sphingolipid G-protein-coupled receptor, 8	Edg8	0.40	0.06	0.08
Neuron differentiation	NM_024125.1	CCAAT/enhancer binding protein (C/EBP), beta	Cebpb	0.31	0.43	0.26
Myelination	X89638.1	Myelin-associated oligodendrocytic basic protein	Mobp	0.35	0.18	0.12
Myelination	NM_017190.1	Myelin-associated glycoprotein	Mag	0.47	0.36	0.29
Myelination	NM_022668.1	Myelin oligodendrocyte glycoprotein	Mog	0.44	0.32	0.19
Myelination	NM_012798.1	Mal, T-cell differentiation protein	Mal	0.37	0.28	0.28
Myelination	AA945178	Signal recognition particle receptor, B subunit transferrin	Srprb Tf	0.33	0.27	0.15
Zinc ion binding	NM_012566.1	Growth factor independent 1 transcription repressor	Gfi1	0.20	0.44	0.41
Zinc ion binding	AW529624	Zinc finger protein 91	Zfp91	0.33	0.32	0.38
Actin binding	AW522439	Ermin, ERM-like protein	Ermn	0.43	0.42	0.28
Apoptosis	BG377720	Solute carrier family 5 (sodium/glucose cotransporter), member 11	Slc5a11	0.25	0.19	0.19
Apoptosis	U21955.1	Eph receptor A	Epha7	0.34	0.48	0.18
Cell Adhesion	BM391100	Mucin 4, cell surface associated	Muc4	0.43	0.36	0.27
Other	AW435010	Protein tyrosine phosphatase, non-receptor type 3	Ptpn3	0.38	0.46	0.36
Other	AF312319.1	gamma-aminobutyric acid (GABA) B receptor 1	Gabbr1	0.33	0.41	0.39
Other	NM_053936.1	Endothelial differentiation, lysophosphatidic acid G-protein-coupled receptor, 2	Edg2	0.47	0.31	0.31

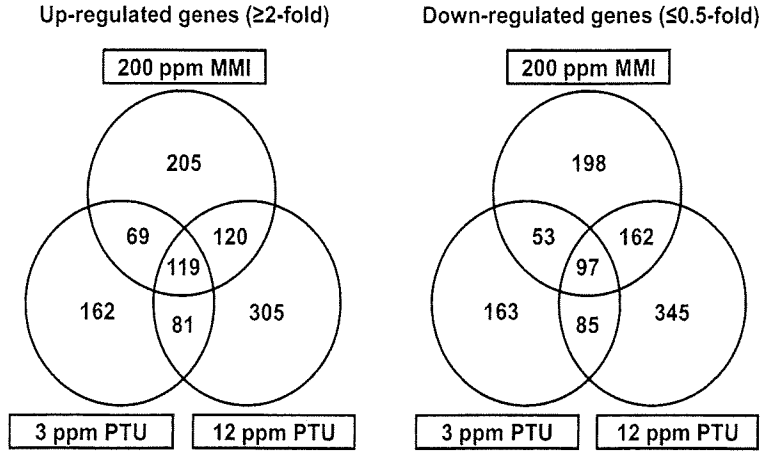

Fig. 2. Venn diagram of gene populations showing altered expression in the hippocampal CA1 pyramidal cell layer at postnatal day 20 in response to maternal exposure to propylthiouracil and/or 2-mercapto-1-methylimidazole compared with the untreated controls. (Left) Up-regulated genes (≥2-fold). (Right) Down-regulated genes (≤0.5-fold). Abbreviations: MMI, 2-mercapto-1-methylimidazole; PTU, 6-propyl-2-thiouracil.

Table 2. Validation of microarray data by real-time RT-PCR

Gene	200 ppm MMI			3 ppm PTU			12 ppm PTU		
	Microarray	Real-time RT-PCR normalized to		Microarray	Real-time RT-PCR normalized to		Microarray	Real-time RT-PCR normalized to	
		Hprt[a]	Gapdh[b]		Hprt	Gapdh		Hprt	Gapdh
Tacr3[c]	7.32 ± 2.21**	4.29 ± 1.27	4.08 ± 1.15*	6.19 ± 2.19**	3.46 ± 1.42	3.76 ± 1.51*	12.49 ± 1.56**	9.23 ± 3.00**	8.81 ± 1.60**
Calb1[d]	4.48 ± 0.66*	3.96 ± 0.74	3.67 ± 0.16	4.85 ± 2.53*	4.74 ± 2.48	4.93 ± 3.79	9.00 ± 1.85**	11.13 ± 2.13**	10.53 ± 3.26**
Slit2[e]	3.04 ± 0.79	2.83 ± 0.90	4.08 ± 1.15*	2.62 ± 1.16	1.33 ± 0.67	3.67 ± 1.51*	7.08 ± 2.15**	4.72 ± 2.57**	8.81 ± 1.60**
Plgl1[f]	3.10 ± 1.57	12.67 ± 5.00	11.5 ± 7.50	4.28 ± 2.88	18.33 ± 6.00	19.00 ± 9.00*	6.86 ± 2.85**	30.67 ± 5.33**	27.00 ± 8.00**
Mobp[g]	0.35 ± 0.15**	0.6 ± 0.22*	0.52 ± 0.16**	0.18 ± 0.07**	0.24 ± 0.07**	0.24 ± 0.05**	0.12 ± 0.02**	0.18 ± 0.04**	0.16 ± 0.04**
Edg8[h]	0.40 ± 0.11*	0.49 ± 0.16*	0.43 ± 0.13*	0.06 ± 0.05**	0.29 ± 0.10**	0.28 ± 0.08**	0.08 ± 0.07**	0.21 ± 0.07**	0.18 ± 0.03**
Cebpb[i]	0.31 ± 0.06**	0.43 ± 0.04**	0.38 ± 0.06**	0.43 ± 0.18**	0.77 ± 0.07	0.76 ± 0.10	0.26 ± 0.04**	0.39 ± 0.16**	0.35 ± 0.22**

a) Hprt, Hypoxanthine-guanine phosphoribosyltransferase; b) Gapdh, Glyceraldehyde 3-phosphate dehydrogenase; c) Tacr3, Tachykinin receptor 3; d) Calb1, Calbindin 1; e) Slit2, Slit homolog 2 (Drosophila); f) Plgl1, Pleomorphic adenoma gene-like 1; g) Mobp, Myelin-associated oligodendrocytic basic protein; h) Edg8, Endothelial differentiation, sphingolipid G-protein-coupled receptor, 8; i) Cebpb, CCAAT/enhancer binding protein (C/EBP), beta.

Values are mean ± SD (n=4) relative to the expression level in the untreated controls. Real-time RT-PCR analysis of Hprt and Gapdh was performed in the analysis of each target gene.

*, **: Significantly different from the untreated controls at $P<0.05$ and $P<0.01$, respectively (Dunnett's multiple comparison test).

tion in response to 12 ppm PTU was approximately 2-fold higher than that with 3 ppm PTU. The number of genes showing up- or down-regulation in response to 200 ppm MMI was in between that elicited by 3 or 12 ppm PTU. One-hundred nineteen genes were up-regulated in common by MMI and PTU, with PTU showing up-regulation from 3 ppm. On the other hand, 97 genes showed down-regulation in all MMI and PTU groups. Representative genes showing up- or down-regulation in all three groups are shown in the Table 1. Among the genes listed, genes associated with nervous system development, zinc ion binding, apoptosis and cell adhesion were commonly up- or down-regulated. Genes related to calcium ion binding were found to be up-regulated and those for myelination were often down-regulated.

Real-time RT-PCR analysis: For confirmation of the microarray data, four genes that were up-regulated and three that were down-regulated in response to anti-thyroid agents were selected for mRNA expression analysis by real-time RT-PCR and the results are summarized in Table 2.

In all exposure groups, many of the expression changes were similar in the two analysis systems, except for much higher expression of *Plagl1* in all exposure groups by real-time RT-PCR as compared with findings from the microarray system.

Although we performed expression analysis of *Efna5* by real-time RT-PCR, expression values were rather low with great variability between samples, and therefore, reliable quantitative data could not be obtained (data not shown).

Immunolocalization of EphA5 and Tacr3 in the hippoc-

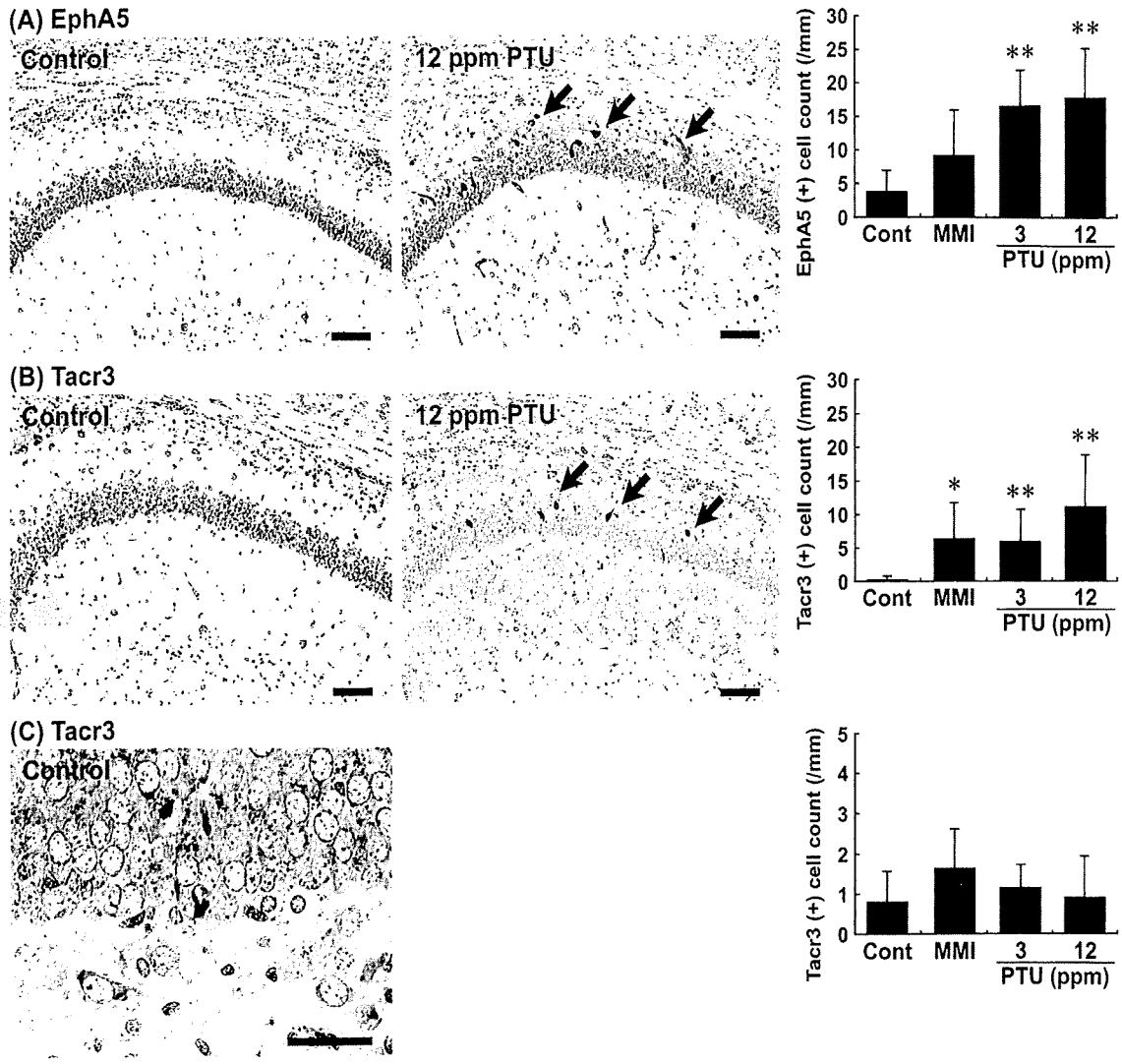

Fig. 3. Distribution of immunoreactive cells for EphA5 and Tacr3 in the hippocampal formation in rats at PND 20 after maternal exposure to anti-thyroid agents. (A) EphA5-immunoreactive cells with strong intensity located within the pyramidal cell layer and stratum oriens of the hippocampal CA1 region (arrows). Note the higher number of EphA5-positive cells in a case exposed to 12 ppm PTU (Right) as compared with the control animal (Left). Bar =100 μm. The graph shows the number of EphA5-positive cells/unit length (mm) of the CA1 region of the bilateral hemispheres. ** $P<0.01$ versus untreated controls (Student's *t*-test). (B) Tacr3-immunoreactive cells with strong intensity located within the pyramidal cell layer and stratum oriens of the hippocampal CA1 region (arrows). Note the higher number of Tacr3-positive cells in a case exposed to 12 ppm PTU (Right) as compared with the control animal (Left). Bar =100 μm. The graph shows the number of Tacr3-positive cells/unit length (mm) of the CA1 region of bilateral hemispheres. * $P<0.05$, ** $P<0.01$ versus untreated controls (Student's *t*-test). (C) Tacr3-immunoreactive cells located in the subgranular zone of the dentate gyrus. Bar =50 μm. The graph shows the number of Tacr3-positive cells/unit length (mm) of the subgranular zone of bilateral hemispheres. Abbreviations: EphA5, Ephrin type A receptor 5; MMI, 2-mercapto-1-methylimidazole; PTU, 6-propyl-2-thiouracil, Tacr3, Tachykinin receptor 3.

ampal formation: Immunohistochemical localization of EphA5 and Tacr3 in the hippocampal formation was examined at PND 20 and PNW 11.

On PND 20, EphA5 showed weak immunoreactivity in the pyramidal neurons throughout the hippocampal formation in the untreated controls. This immunoreactivity was unchanged by exposure to anti-thyroid agents. On the other hand, very sparse distribution of strongly immunoreactive cells for EphA5 was observed in the region of the CA1 pyramidal cell layer and stratum oriens in the untreated control animals, but immunoreactive cells were significantly increased showing scattered distribution by PTU at both 3 and 12 ppm (Fig. 3A). MMI-exposed animals also showed a small increase in the number of strongly positive cells with EphA5. Increased intensity in immunoreactivity of EphA5 was also observed in the gray matter consisting of neuropil at the stratum oriens of the CA1 region (Fig. 3A), and also in the molecular layer of the dentate gyrus at PND 20 after exposure to anti-thyroid agents, especially in PTU-exposed groups (data not shown).

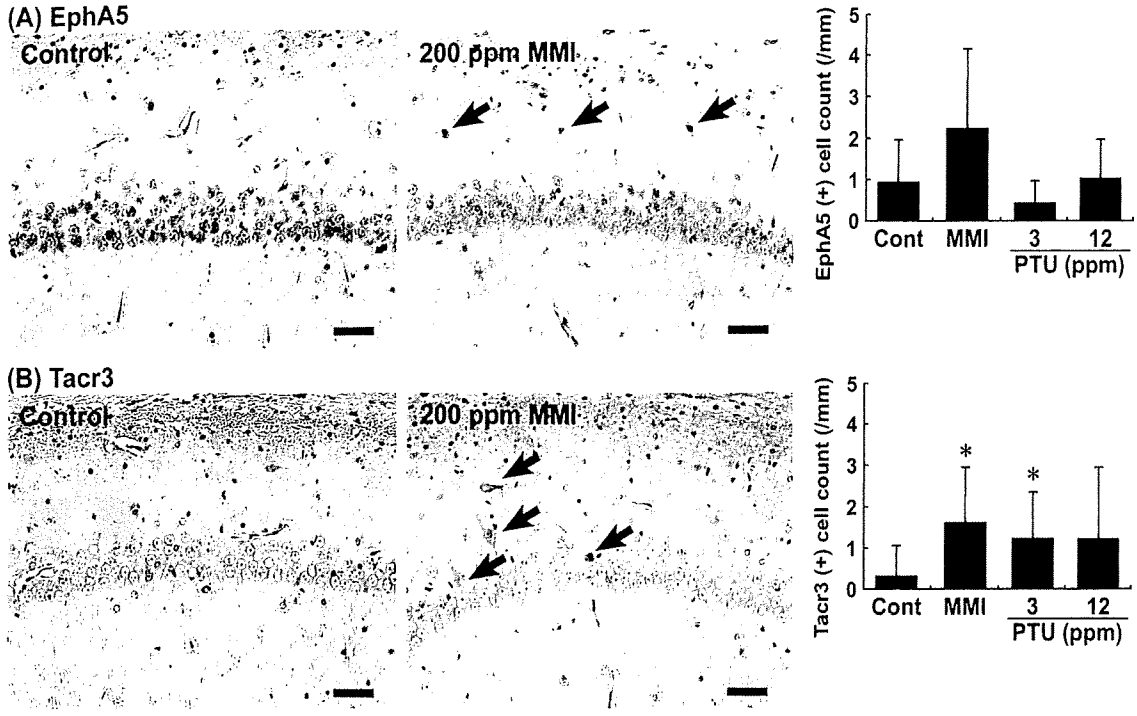

Fig. 4. Distribution of immunoreactive cells for EphA5 and Tacr3 in the hippocampal formation at PNW 11 of rats exposed maternally to anti-thyroid agents. (A) EphA5-immunoreactive cells with moderate staining intensity located within the pyramidal cell layer and stratum oriens of the hippocampal CA1 region. EphA5-positive cells in a case exposed to 200 ppm MMI (Right) as compared with the control animal (Left). The arrows show positive cells. Bar =50 μm. The graph shows the number of EphA5-positive cells/unit length (mm) of the CA1 region of the bilateral hemispheres. (B) Tacr3-immunoreactive cells with weak to moderate staining intensity located within the pyramidal cell layer and stratum oriens of the hippocampal CA1 region (arrows). Immunoreactivity is rather faint as compared with that observed at PND 20. Note the higher number of Tacr3-positive cells in a case exposed to 200 ppm MMI (Right) as compared with the control animal (Left). Bar =50 μm. The graph shows the number of Tacr3-positive cells/unit length (mm) of the CA1 region of bilateral hemispheres. * $P<0.05$ versus untreated controls (Student's t-test). Abbreviations: EphA5, Ephrin type A receptor 5; MMI, 2-mercapto-1-methylimidazole; PTU, 6-propyl-2-thiouracil; Tacr3, Tachykinin receptor 3.

With regards to Tacr3, the number of positive cells was increased with a scattered distribution showing strong intensity in the CA1 region similarly to that of EphA5 in the animals exposed to MMI or PTU on PND 20, but they were mostly absent in the untreated controls (Fig. 3B). Similarly, Tacr3-immunoreactive cells were sparse in the subgranular zone of the dentate gyrus in the MMI and PTU-exposed animals and in the untreated controls, but there were no differences in the number of positive cells as compared with the untreated controls (Fig. 3C). In addition, increased intensity in neuropil-immunoreactivity of Tacr3 was also observed in the strata oriens and radiatum of the CA1 region in all exposure groups of anti-thyroid agents (Fig. 3B).

On PNW 11, EphA5 showed weak immunoreactivity in the pyramidal neurons throughout the hippocampal formation in the untreated controls. This immunoreactivity was unchanged by exposure to anti-thyroid agents. EphA5-immunoreactive cells with moderate staining intensity were very sparsely observed in the region of the CA1 pyramidal cell layer and stratum oriens in the untreated control animals. There was no statistically significant increase in the number of these immunoreactive cells after exposure to PTU, while animals exposed to MMI showed a tendency for an increased number of immunoreactive cells (Fig. 4A). Increased neuropil-immunoreactivity of EphA5 as observed at PND 20 in exposure groups of anti-thyroid agents was mostly disappeared at PNW 11 (data not shown).

As well as at PND 20, Tacr3-immunoreactive cells were mostly absent in the untreated controls at PNW 11; however, a few immunoreactive cells with weak to moderate intensity were observed in the stratum oriens of the CA1 region in the animals exposed to anti-thyroid agents. There was a statistically significant difference in the animals treated with MMI or 3 ppm PTU compared with the untreated controls (Fig. 4B). Although the change was non-significant and lacked dose-dependence, 12 ppm PTU also showed an increasing tendency in the number of Tacr3-immunoreactive cells. In addition, increased neuropil-immunoreactivity of Tacr3 as observed at PND 20 in exposure groups of anti-thyroid agents was mostly disappeared at PNW 11 (data not shown).

DISCUSSION

In our recent study using rats [24], after maternal exposure to MMI or PTU, we detected typical hypothyroidism-related changes in the thyroid-related hormone levels, and hippocampal CA1 pyramidal neurons due to neuronal mismigration, as previously reported [8]. We also observed white matter changes, which seem to be due to impaired oligodendroglial development [6, 21]. To visualize molecules related to impaired neuronal development, microdissected CA1 region-specific global gene expression profiling was performed in the present study using the same animals that were used in our previous study. Two recently published studies have used microarrays to examine the expression profiles in the cerebral cortex and hippocampus of genes linked to developmental hypothyroidism caused by maternal PTU-exposure [7, 19]. In accordance with these studies, the genes that were significantly down-regulated in the present study included those that play roles in myelination, such as *Mobp* and myelin-associated glycoprotein, suggestive of the reflection of suppressed myelination by developmental hypothyroidism [21]. However, the genes that were found to be up-regulated on microdissected CA1 pyramidal cell layer, including *Efna5* and *Tacr3*, in the present study, have not been identified in previous studies. This difference may be related to the target tissues collected and the methods used, including microdissection of CA1 pyramidal cell layer from paraffin-embedded sections in the present study versus manual dissection of the cortical tissues from unfixed tissues in the previous studies.

EphA5 is a tyrosine kinase receptor that is almost exclusively expressed in the nervous system [15]. EphA5 and its ligand are important in mediating axon guidance, topographic projection, development, cell migration and the plasticity of limbic structures [15]. In addition, the transient expression of EphA5 during development is correlated with early neurogenesis and the migration of differentiated cells in the midbrain [3]. Thus, although expression of EphA5 was mostly weak in the euthyroid CA1 pyramidal neurons at PND 20, the increased number of EphA5-expressing cells with strong intensity in the CA1 region during developmental hypothyroidism in the present study reflects the neuronal mismigration caused by anti-thyroid agents. However, this increase was recovered after cessation of developmental hypothyroidism. Ephrins and their receptors are recently identified molecules and functional relationship between subfamily proteins is largely unknown; however, we, in the present study, found down-regulation of Epha7, another subfamily ephrin receptor, in all exposure groups of anti-thyroid agents (Table 1).

Tacr3, a member of the mammalian tachykinin peptide neurotransmitter/neuromodulator receptor family, is predominantly expressed in neurons in both the peripheral and central nervous systems, including the hippocampus [25]. There is increasing evidence of the role of Tacr3 on the survival and function of dopaminergic neurons. The survival of mesencephalic dopaminergic neurons during development largely depends on excitatory inputs, and tachykinins, through their receptors, are reported to play role in excitation [20]. On the other hand, senktide, a Tacr3 agonist, activates dopaminergic neurons to stimulate the release of dopamine and serotonin, and hyperlocomotion in gerbils [14]. Abnormal excitatory action of D_2-like receptor, one of the major subtypes of dopaminergic receptors, was observed on glutamatergic transmission in the CA1 synapses in the adult stage of rats after developmental hypothyroidism, suggesting a permanent disruption of synaptic integration in the CA1 neural networks [16]. While the role of Tacr3 in the hippocampal CA1 region during development is not clear, the increase in Tacr3-positive cells with strong intensity in this region during developmental hypothyroidism suggests a cell survival effect of tachykinin-3. Although the magnitude of the change was decreased, as compared with that at the end of the developmental hypothyroidism, the increased number of Tacr3-positive cells in the CA1 region of MMI and 3 ppm PTU-exposed animals may be an outcome of permanent disruption of synaptic integration, as described by Oh-Nishi *et al.* [16]. However, sparse distribution of Tacr3-positive cells may reflect that impairment sustained in a small population of aberrantly migrated neurons.

In conclusion, in this study, we have shown gene expression profiles showing altered expression in response to developmental hypothyroidism by analysis on microdissected hippocampal CA1 pyramidal cell layer in rats. Immunohistochemical analysis of the two candidate molecules revealed that developmental hypothyroidism until weaning is associated with the persistence of Tacr3-expressing neurons until the adult stage in the CA1 region, suggestive of the reflection of permanent disruption of synaptic integration. These findings probably reflect a mechanism to facilitate cell survival of aberrantly developed neurons due to mismigration.

ACKNOWLEDGMENT(S). We thank Miss Tomomi Morikawa for her technical assistance in conducting the animal study. We also thank Mrs. Shigeko Suzuki and Miss Ayako Kaneko for their technical assistance in preparing the histological specimens. This work was supported in part by Health and Labour Sciences Research Grants (Research on Risk of Chemical Substances) from the Ministry of Health, Labour and Welfare of Japan. All of the authors disclose that there are no conflicts of interest that could inappropriately influence the outcomes of the present study.

REFERENCES

1. Akaike, M., Kato, N., Ohno, H. and Kobayashi, T. 1991. Hyperactivity and spatial maze learning impairment of adult rats with temporary neonatal hypothyroidism. *Neurotoxicol. Teratol.* **13**: 317–322.
2. Comer, C. P. and Norton, S. 1982. Effects of perinatal methimazole exposure on a developmental test battery for neurobehavioral toxicity in rats. *Toxicol. Appl. Pharmacol.* **63**: 133–141.
3. Cooper, M. A., Crockett, D. P., Nowakowski, R. S., Gale, N. W. and Zhou, R. 2009. Distribution of EphA5 receptor protein

in the developing and adult mouse nervous system. *J. Comp. Neurol.* **514**: 310–328.
4. de Escobar, G. M., Obregón, M. J. and del Rey, F. E. 2007. Iodine deficiency and brain development in the first half of pregnancy. *Public Health Nutr.* **10**: 1554–1570.
5. Gerlai, R., Shinsky, N., Shih, A., Williams, P., Winer, J., Armanini, M., Cairns, B., Winslow, J., Gao, W. and Phillips, H. S. 1999. Regulation of learning by EphA receptors: a protein targeting study. *J. Neurosci.* **19**: 9538–9549.
6. Goodman, J. H. and Gilbert, M. E. 2007. Modest thyroid hormone insufficiency during development induces a cellular malformation in the corpus callosum: a model of cortical dysplasia. *Endocrinology* **148**: 2593–2597.
7. Kobayashi, K., Akune, H., Sumida, K., Saito, K., Yoshioka, T. and Tsuji, R. 2009. Perinatal exposure to PTU decreases expression of Arc, Homer 1, Egr 1 and Kcna 1 in the rat cerebral cortex and hippocampus. *Brain Res.* **1264**: 24–32.
8. Lavado-Autric, R., Ausó, E., García-Velasco, J. V., Arufe Mdel, C., Escobar del Rey, F., Berbel, P. and Morreale de Escobar, G. 2003. Early maternal hypothyroxinemia alters histogenesis and cerebral cortex cytoarchitecture of the progeny. *J. Clin. Invest.* **111**: 954–957.
9. Lee, K-Y., Shibutani, M., Inoue, K., Kuroiwa, K., U, M., Woo, G-H. and Hirose, M. 2006. Methacarn fixation—Effects of tissue processing and storage conditions on detection of mRNAs and proteins in paraffin-embedded tissues. *Anal. Biochem.* **351**: 36–43.
10. Masutomi, N., Shibutani, M., Takagi, H., Uneyama, C., Takahashi, N. and Hirose, M. 2003. Impact of dietary exposure to methoxychlor, genistein, or diisononyl phthalate during the perinatal period on the development of the rat endocrine/reproductive systems in later life. *Toxicology* **192**: 149–170.
11. Mileusnic, D., Lee, J. M., Magnuson, D. J., Hejna, M. J., Krause, J. E., Lorens, J. B. and Lorens, S. A. 1999. Neurokinin-3 receptor distribution in rat and human brain: an immunohistochemical study. *Neuroscience* **89**: 1269–1290.
12. Montero-Pedrazuela, A., Venero, C., Lavado-Autric, R., Fernández-Lamo, I., García-Verdugo, J. M., Bernal, J. and Guadaño-Ferraz, A. 2006. Modulation of adult hippocampal neurogenesis by thyroid hormones: implications in depressive-like behavior. *Mol. Psychiatry* **11**: 361–371.
13. Nakamura, R., Teshima, R., Hachisuka, A., Sato, Y., Takagi, K., Nakamura, R., Woo, G-H., Shibutani, M. and Sawada, J. 2007. Effects of developmental hypothyroidism induced by maternal administration of methimazole or propylthiouracil on the immune system of rats. *Int. Immunopharmacol.* **7**: 1630–1638.
14. Nordquist, R. E., Durkin, S., Jacquet, A. and Spooren, W. 2008. The tachykinin NK3 receptor agonist senktide induces locomotor activity in male Mongolian gerbils. *Eur. J. Pharmacol.* **600**: 87–92.
15. Numachi, Y., Yoshida, S., Yamashita, M., Fujiyama, K., Toda, S., Matsuoka, H., Kajii, Y. and Nishikawa, T. 2007. Altered EphA5 mRNA expression in rat brain with a single methamphetamine treatment. *Neurosci. Lett.* **424**: 116–121.
16 Oh-Nishi, A., Saji, M., Furudate, S. I. and Suzuki, N. 2005. Dopamine D_2-like receptor function is converted from excitatory to inhibitory by thyroxine in the developmental hippocampus. *J. Neuroendocrinol.* **17**: 836–845.
17. Olivieri, G. and Miescher, G. C. 1999. Immunohistochemical localization of EphA5 in the adult human central nervous system. *J. Histochem. Cytochem.* **47**: 855–861.
18. Porterfield, S. P. 2000. Thyroidal dysfunction and environmental chemicals—Potential impact on brain development. *Environ. Health Perspect.* **108**: 433–438.
19. Royland, J. E., Parker, J. S. and Gilbert, M. E. 2008. A genomic analysis of subclinical hypothyroidism in hippocampus and neocortex of the developing rat brain. *J. Neuroendocrinol.* **20**: 1319–1338.
20. Salthun-Lassalle, B., Traver, S., Hirsch, E. C. and Michel, P. P. 2005. Substance P, neurokinins A and B, and synthetic tachykinin peptides protect mesencephalic dopaminergic neurons in culture via an activity-dependent mechanism. *Mol. Pharmacol.* **68**: 1214–1224.
21. Schoonover, C. M., Seibel, M. M., Jolson, D. M., Stack, M. J., Rahman, R. J., Jones, S. A., Mariash, C. N. and Anderson, G. W. 2004 Thyroid hormone regulates oligodendrocyte accumulation in developing rat brain white matter tracts. *Endocrinology* **145**: 5013–5020.
22. Shibutani, M., Uneyama, C., Miyazaki, K., Toyoda, K. and Hirose, M. 2000. Methacarn fixation: a novel tool for analysis of gene expressions in paraffin-embedded tissue specimens. *Lab. Invest.* **80**: 199–208.
23. Shibutani, M., Lee, K-Y., Igarashi, K., Woo, G-H., Inoue, K., Nishimura, T. and Hirose, M. 2007. Hypothalamus region-specific global gene expression profiling in early stages of central endocrine disruption in rat neonates injected with estradiol benzoate or flutamide. *Dev. Neurobiol.* **67**: 253–269.
24. Shibutani, M., Woo, G-H., Fujimoto, H., Saegusa, Y., Takahashi, M., Inoue, K., Hirose, M. and Nishikawa, A. 2009. Assessment of developmental effects of hypothyroidism in rats from in utero and lactation exposure to anti-thyroid agents. *Reprod. Toxicol.* **28**: 297–307.
25. Smith, P. W. and Dawson, L. A. 2008. Neurokinin 3 (NK3) receptor modulators for the treatment of psychiatric disorders. *Recent Pat. CNS Drug Discov.* **3**: 1–15.
26. Takagi, H., Shibutani, M., Kato, N., Fujita, H., Lee, K-Y., Takigami, S., Mitsumori, K. and Hirose, M. 2004. Microdissected region-specific gene expression analysis with methacarn-fixed, paraffin-embedded tissues by real-time RT-PCR. *J. Histochem. Cytochem.* **52**: 903–913.
27. Uneyama, C., Shibutani, M., Masutomi, N., Takagi, H. and Hirose, M. 2002. Methacarn fixation for genomic DNA analysis in microdissected, paraffin-embedded tissue specimens. *J. Histochem. Cytochem.* **50**: 1237–1245.
28. Woo, G-H., Takahashi, M., Inoue, K., Fujimoto, H., Igarashi, K., Kanno, J., Hirose, M., Nishikawa, A. and Shibutani, M. 2009. Cellular distributions of molecules with altered expression specific to thyroid proliferative lesions developing in a rat thyroid carcinogenesis model. *Cancer Sci.* **100**: 617–625.

NANOS2 interacts with the CCR4-NOT deadenylation complex and leads to suppression of specific RNAs

Atsushi Suzuki[a], Katsuhide Igarashi[b], Ken-ichi Aisaki[b], Jun Kanno[b], and Yumiko Saga[c,1]

[a]Interdisciplinary Research Center, Yokohama National University, Yokohama, Kanagawa 240-8501, Japan; [b]Cellular and Molecular Toxicology Division, National Institute of Health Sciences, Setagayaku, Tokyo 158-8501, Japan; and [c]Division of Mammalian Development, National Institute of Genetics, Mishima 411-8540, Japan

Edited by Ruth Lehmann, New York University Medical Center, New York, NY, and approved December 30, 2009 (received for review August 2, 2009)

Nanos is one of the evolutionarily conserved proteins implicated in germ cell development. We have previously shown that NANOS2 plays an important role in both the maintenance and sexual development of germ cells. However, the molecular mechanisms underlying these events have remained elusive. In our present study, we found that NANOS2 localizes to the P-bodies, known centers of RNA degradation that are abundantly accumulated in male gonocytes. We further identified by immunoprecipitation that the components of the CCR4-NOT deadenylation complex are NANOS2-interacting proteins and found that NANOS2 promotes the localization of CNOT proteins to P-bodies in vivo. We also elucidated that the NANOS2/CCR4-NOT complex has deadenylase activity in vitro, and that some of the RNAs implicated in meiosis interact with NANOS2 and are accumulated in its absence. Our current data thus indicate that the expression of these RNA molecules is normally suppressed via a NANOS2-mediated mechanism. We propose from our current findings that NANOS2-interacting RNAs may be recruited to P-bodies and degraded by the enzymes contained therein through NANOS2-mediated deadenylation.

germ cells | P-body | meiosis

In the mouse, the primordial germ cells (PGCs) are segregated from the somatic cell lineage at an early gastrulation stage (1). Although the PGCs are potent producers of both oogonia and spermatogonia, sexual differentiation is induced after their colonization of the embryonic gonads with somatic cells. However, the initial steps leading to diversification of these cells have long remained unsolved. Retinoic acid (RA) signaling has recently been identified as the initial trigger for feminization (2). RA molecules derived from the mesonephros trigger meiotic initiation in female gonocytes via the induction of the RA responsive gene *Stra8*, which is required for premeiotic replication (3). In contrast, male gonocytes are protected from exposure to RA by CYP26B1, an RA metabolizing enzyme produced from somatic cells, resulting in the suppression of meiosis up to E13.5 (4, 5). In addition, *Nanos2* expression begins after E13.5 and is required for the maintenance and promotion of the male germ cell state (6).

Nanos is an evolutionarily conserved RNA-binding protein that is essential for germ cell development (7). In *Drosophila*, Nanos forms a complex with another RNA-binding protein, Pumilio, and represses the translation of the *hunchback*, *cyclin B,* and *hid* mRNAs thereby establishing embryonic polarity, mitotic quiescence, and suppression of apoptosis, respectively (8–10). Three *Nanos* homologs, *Nanos1–3*, exist in the mouse, among which *Nanos3* and *Nanos2* are expressed in the germ cells and are required to protect these cells from undergoing apoptosis during migration and after colonization of the male gonads, respectively (11, 12). In addition, *Nanos2* plays a key role during the sexual development of germ cells by suppressing meiosis and promoting male-type differentiation in the embryonic male gonads. Moreover, the forced expression of *Nanos2* in female gonocytes can induce the suppression of meiosis and promotion of male-type gene expression (6). However, the molecular mechanisms underlying how this protein accomplishes such pleiotropic functions in the mouse germ cells remain unknown.

In our present study, we find that NANOS2 localizes to P-bodies, a central hub of RNA degradation (13, 14). We further identify components of the CCR4-NOT deadenylation complex as NANOS2-associated proteins in vivo, which can cleave poly(A) RNA in vitro. We also show that specific mRNAs interact with NANOS2, and thus propose that NANOS2 plays a role in recruiting the CCR4-NOT deadenylation complex to trigger the degradation of specific RNAs.

Results

NANOS2 Localizes at P-Bodies During Gonocyte Development. To increase our understanding of the molecular mechanisms underlying the function of the NANOS2 protein, we first analyzed the cellular localization of this protein by immunostaining. Consistent with the results of our previous western analyses (15), NANOS2 protein was first detectable at E13.5 in the cytoplasm of male mouse gonocytes. This signal intensity increased until about E16.5 and then slightly decreased by E17.5. In addition, we found that some of the NANOS2 proteins formed discrete foci, the number of which gradually increased until E16.5 and then decreased thereafter (Fig. S1 *A–F*). Because *Drosophila* Vasa and Tudor are known to form cytoplasmic foci (16, 17), which are the polar granules in the germ plasm, we speculated that these NANOS2 foci might colocalize with the mouse homologs of Vasa, MVH (mouse vasa homolog) (18) and the Tudor protein TDRD1 (tudor domain containing 1) (19). However, these foci did not show any clear colocalization with NANOS2 (Fig. S2 *A–F*). We next tested the possibility that the NANOS2 foci might correspond to P-bodies, which are known to function as a center of RNA degradation. We thus conducted double-immunostaining using antibodies against the P-body components DCP2 and XRN1, an mRNA decapping enzyme and RNA exonuclease, respectively (13, 14). We were initially surprised to find that many P-bodies could be specifically observed only in germ cells and not in the somatic cells in E15.5 male gonads, and also that the NANOS2 foci clearly merged with those of DCP2 and XRN1 (Fig. 1 *A–F*) from E13.5 to E17.5 (Fig. S3 *A–F*). This suggests the possibility that NANOS2 may be involved in RNA degradation.

Nanos2 Functions in the Formation of P-Bodies. We further examined the status of the P-bodies in the mouse gonads of both sexes by immunostaining of p54/RCK, a homolog of *Drosophila* Me31B and also a marker of these structures (20). Although the P-bodies seemed to be present in the same number and size in the gonocytes of both sexes at E12.5, they were gradually reduced and eventually lost by E14.5 in female gonocytes (Fig. S4 *E* and *F*). In contrast, the P-bodies become much larger in both number and

Author contributions: A.S. and Y.S. designed research; A.S., performed research; K.I., K.. A., and J.K. analyzed data of microarray analyses; and A.S. and Y.S. wrote the paper.

The authors declare no conflict of interest.

This article is a PNAS Direct Submission.

[1]To whom correspondence should be addressed. E-mail: ysaga@lab.nig.ac.jp.

This article contains supporting information online at www.pnas.org/cgi/content/full/0908664107/DCSupplemental.

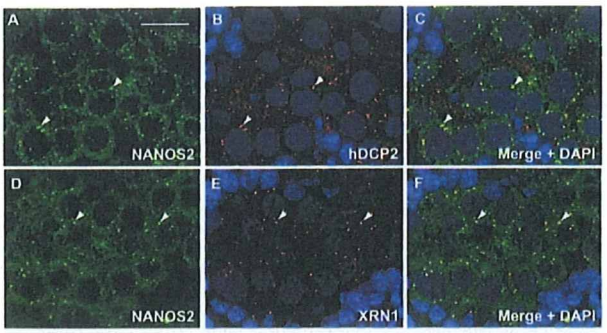

Fig. 1. NANOS2 localizes to the P-bodies in male mouse gonocytes. (*A–L*) Sections prepared from wild-type E15.5 male gonads were double-stained with mouse anti-NANOS2 (green) (*A* and *D*) and either hDCP2 (*B*) or mXRN1 (*E*) antibodies (red staining in each case). Arrowheads indicate colocalization of NANOS2 and hDCP2 (C) or XRN1 (*F*). DNA was counterstained with DAPI (blue). (Scale bar in *A*, 20 μm for all panels.)

size from E14.5, concomitant with the onset of NANOS2 expression, in male gonocytes (Fig. S4 *A–D*).

To further explore the role of NANOS2 in P-body formation, we examined the status of these structures in the absence of *Nanos2*. Although there were, somewhat unexpectedly, many P-bodies detected in both *Nanos2*$^{+/-}$ and *Nanos2*$^{-/-}$ male gonocytes at E13.5, their sizes became gradually larger, whereas their number became smaller, at the later stages of embryogenesis in the absence of *Nanos2* (Fig. 2*A–D*). This was also observed in *Nanos2, Bax* double-null male gonocytes (Fig. 2 *E* and *F*), where apoptotic cell death was suppressed, suggesting that apoptosis does not affect P-body status. This indicates that NANOS2 is not essential for the assembly of P-bodies but is required for the maintenance of their normal state. To further elucidate the functions of NANOS2 in P-body formation, we also examined the status of the P-bodies in NANOS2-expressing female gonocytes (6). Although they could not be detected in normal female gonocytes at E16.5, we found many P-bodies in NANOS2-expressing female cells and additionally observed that NANOS2 localizes at the P-bodies in these cells (Fig. 2 *G–I*). These data indicate that NANOS2 is sufficient to maintain the number of P-bodies when female gonocytes have acquired a male-type phenotype due to NANOS2 expression.

NANOS2 Interacts with the CCR4-NOT Deadenylation Complex and Regulates Its Localization. To explore the molecular functions of NANOS2, we searched for proteins that interact with it. To this end, we prepared male gonadal extracts from *Nanos2*$^{+/-}$ and *Nanos2*$^{-/-}$ embryos at E14.5 and subjected them to immunoprecipitation with anti-NANOS2 antibodies. We found that two major bands of more than 200 kDa were exclusively precipitated from *Nanos2*$^{+/-}$ gonads, and by mass spectrometric analysis identified these products as CNOT1, a component of the CCR4-NOT deadenylation complex (13) (Fig. 3A).

In further immunoprecipitation experiments, we used a transgenic mouse line expressing a FLAG-tagged NANOS2 under the direct control of the *Nanos2* enhancer (15) (Fig. S5*A*), since we had confirmed that this fusion protein was functional (Fig. S5 *B–F*) and localized at the P-bodies (Fig. S5 *G–I*). Western analyses revealed that CNOT1 coprecipitates with FLAG-tagged NANOS2 (Fig. 3*B, Upper*), confirming the results of our mass spectrometric analysis. We also found that other components of the CCR4-NOT complex, CNOT3, CNOT6L/Ccr4b, CNOT7/Caf1a, and CNOT9/Rcd1 (13, 21), also coprecipitated with FLAG-tagged NANOS2, indicating that NANOS2 associates with the CCR4-NOT deadenylation complex in vivo. We additionally found that this interaction is independent of RNA, as the levels of coprecipitated CNOT proteins were not affected by treatments with RNase (Fig. 3*B*). Finally, these CNOT proteins were found to colocalize with NANOS2 in P-bodies (Fig. 3 *C–E* and Fig. S6 *A–I*), suggesting that this complex may play a role in the activities of these elements.

To better understand the physiological significance of its interaction with NANOS2, we investigated the localization of CCR4-NOT deadenylation complex in *Nanos2*$^{-/-}$ male gonads by immunostaining CNOT proteins with DCP1A, another decapping enzyme and also a component of P-bodies (13, 14). Although CNOT3 was found to clearly localize to P-bodies in *Nanos2*$^{+/-}$ male gonads (Fig. 3 *F–H*), we detected only weak signals for this protein in P-bodies in the absence of NANOS2 (Fig. 3 *I–K*) even though the levels of CNOT3 are not reduced in *Nanos2*$^{-/-}$ male gonads (Fig. 3*L*). We obtained similar results for CNOT1 (Fig. S7). These data suggest that NANOS2 promotes the localization of the CCR4-NOT deadenylation complex to P-bodies, although a subpopulation of this complex still remains in these structures in the absence of NANOS2, possibly via a NANOS2-independent mechanism. Based on these findings and the fact that the CCR4-NOT deadenylation complex regulates the first step of mRNA degradation (22), we speculate that NANOS2 recruits this deadenylation complex to P-bodies where it promotes the degradation of RNAs.

Complex of NANOS2 and CCR4-NOT Deadenylation Complex in Male Germ Cells Retains Deadenylase Activity. To address the critical question of whether NANOS2-interacting deadenylase actually has catalytic activity, we used NANOS2-overexpressing (NANOS2 O/E) adult testes to obtain sufficient amounts of this protein and thus overcome the limitations of using embryonic testis in biochemical analyses. In the testis of the postnatal mouse, NANOS2 is expressed in a small population of undifferentiated spermatogonia (23) and localizes to P-bodies (Fig. S8 *A–C*) as in the male gonocytes. This expression is subsequently lost as these cells differentiate. However, if FLAG-tagged NANOS2 is forcedly and continuously expressed in the spermatogonial population, the male mouse become infertile because the spermatogonia remain in an undifferentiated state in the testis, in which a large number of NANOS2-positive spermatogonia occupy the periphery of the seminiferous tubules (23). In addition, FLAG-tagged NANOS2 also localizes to the P-bodies in the spermatogonia in the manner similar to endogenous Nanos2 (Fig. S8 *D–F*). We prepared testis extracts from this mouse and performed immunoprecipitations with anti-FLAG antibodies and control IgG, and then subjected these immunoprecipitates to in vitro deadenylase assay (21) (Fig. 4*A*). As shown in Fig. 4*B*, cleavage of the poly(A) RNA substrate occurred only with NANOS2 immunoprecipitates, which also contains the CNOT6L and CNOT7 catalytic components of the deadenylation complex (Fig. 4*C*). These results lead us to propose that NANOS2 promotes the degradation of NANOS2-interacting mRNAs through the deadenylase activity of the CCR4-NOT complex.

NANOS2 Interacts with Specific mRNAs and May Promote Their Degradation. Based on our working hypothesis, we further speculated that (*i*) the NANOS2 complex should contain specific mRNAs that would be degraded via NANOS2-mediated deadenylation, such that (*ii*) the expression levels of these transcripts would be low in wild-type male gonocytes but up-regulated in the absence of NANOS2. To test these possibilities, RNAs that coprecipitated with FLAG-tagged NANOS2 were purified and subjected to RT-PCR. Because we had previously shown that male gonocytes could enter meiosis in the absence of NANOS2, it was plausible that mRNAs involved in meiosis might be directly suppressed through NANOS2-mediated RNA degradation. As expected, *Sycp3*, *Stra8*, *Taf7l*, *Dazl*, and *Meisetz* (3, 24–27) transcripts that are implicated in meiosis were specifically detected only in the NANOS2 protein precipitates despite their very low expression in male gonads (Fig. 5 *A* and *B*). In contrast, the

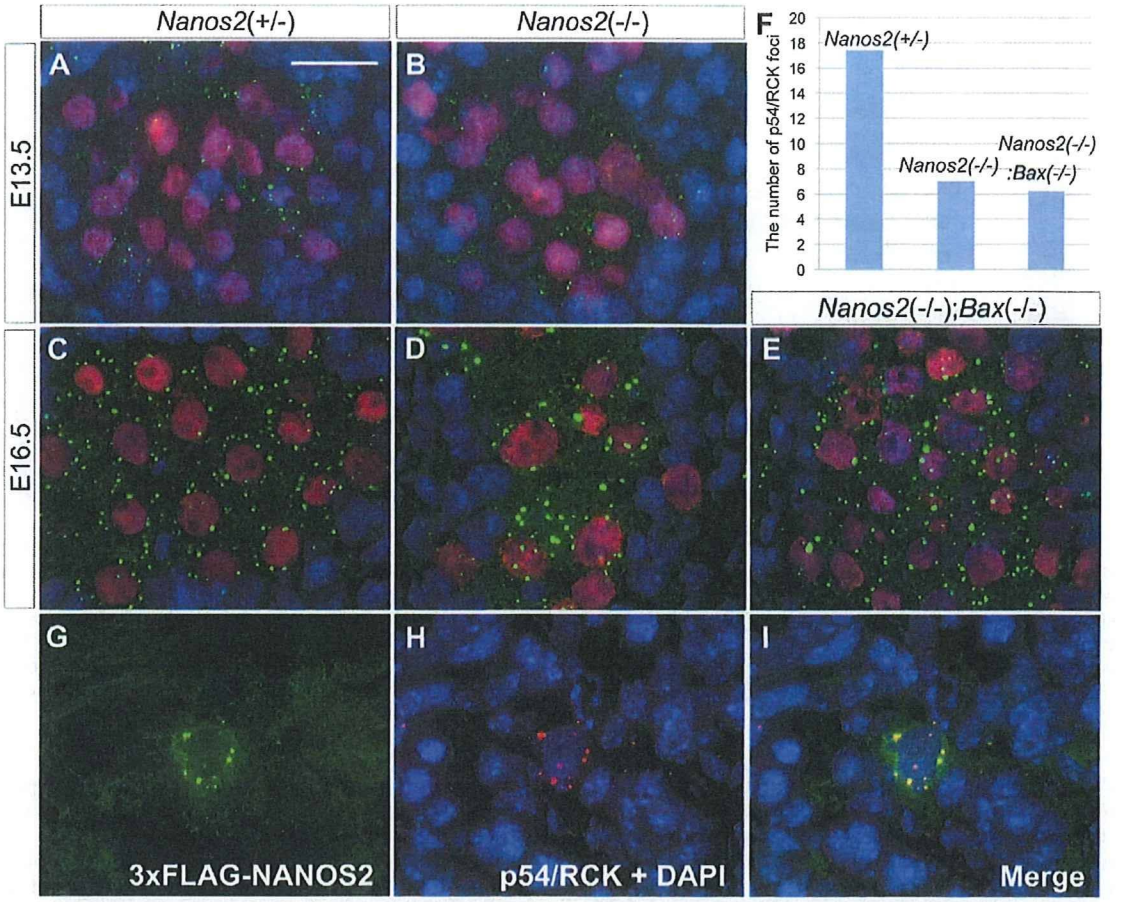

Fig. 2. Functional role of NANOS2 during the formation of the P-bodies. (*A–E*) Male gonadal sections from *Nanos2*$^{+/-}$ (*A* and *C*), *Nanos2*$^{-/-}$ (*B* and *D*), and *Nanos2*$^{-/-}$*Bax*$^{-/-}$ (*E*) embryos at stages E13.5 (*A* and *B*), and E16.5 (*C, D,* and *E*) were immunostained with p54/RCK (green) and TRA98 (red) antibodies. (*F*) Average number of p54/RCK foci per male gonocyte at E16.5 was quantified in each picture using ImageJ software (National Institutes of Health) and a cell counter, with the foci of less than a 20 permission value excluded using Photoshop (Adobe). The data shown correspond to two to three pictures. (*G–I*) A female gonadal section from a NANOS2-expressing embryo at E16.5 was immunostained with anti-FLAG (green) (*G*) and anti-p54/RCK (red) (*H*) antibodies. DNA was counterstained using DAPI (blue). (Scale bar in *A*, 20μm for *A–E* and *G–I*.)

G3pdh, *Dnmt3l* and *Dnmt3a* mRNAs did not show specific accumulation in the NANOS2 precipitates although they are all highly expressed in male gonads. These data indicate that the mRNAs involved in meiosis specifically interact with NANOS2 in vivo.

We next investigated global changes in gene expression upon the loss of *Nanos2* using comparative GeneChip analyses (Table S1). The resulting scatter plots showed that many genes become up- or down-regulated in *Nanos2*$^{-/-}$ male gonads by E15.5 (Fig. S9 *A–C*). For example, we found that the genes highly expressed only in male gonocytes, such as *Dnmt3l*, *Tdrd1* and *Miwi2*/*Piwi-like 4* (19, 28, 29), are down-regulated in the *Nanos2*$^{-/-}$ male gonads, whereas *Figla*, *Lhx8* and *Nobox*, which have been shown to be essential only for oogenesis and not for spermatogenesis (30–32), become accumulated in the *Nanos2*$^{-/-}$ male gonads (6) (Fig. S9 *D–I*). These results suggest that male gonocytes cannot enter the male pathways and become feminized by the up-regulation of female-type genes. In addition, and consistent with the results of our immunoprecipitation assay, *Sycp3*, *Stra8*, *Taf7l*, *Dazl,* and *Meisetzs* mRNAs were also found to be up-regulated in *Nanos2*$^{-/-}$ male gonads (Fig. 5 *C–G*). Our current findings thus indicate that NANOS2-interacting mRNAs become accumulated if NANOS2 is absent in male gonocytes, which in turn indicates that NANOS2 might be indirectly affecting the transcription of these genes, or that they are normally suppressed in wild-type male gonocytes through a NANOS2-directed mechanism, possibly a deadenylation pathway.

Discussion

Molecular Role of NANOS2. In our current study, we show that the CCR4-NOT deadenylation complex is coprecipitated with NANOS2 from male gonadal extracts. This is the first evidence that the interaction between a Nanos homolog and the CCR4-NOT deadenylation complex exists *in vivo,* although it has been shown using a yeast two-hybrid system that *Drosophila* Nanos can directly and potently bind to NOT4, a component of the CCR4-NOT complex (33). Hence, as suggested previously by Kadyrova et al. for *Drosophila* Nanos, and as confirmed by our present analyses in vivo, the recruitment of the CCR4-NOT deadenylation complex to target mRNAs may be a conserved function of the Nanos proteins.

We also found that NANOS2 localizes to P-bodies in the male gonocytes and adult mouse spermatogonia. P-bodies are known to be a central hub of RNA degradation, in which decapping enzymes and exonucleases are also localized. However, emerging evidence in other systems suggests that P-bodies not only function to degrade RNAs but also to store mRNAs in a translationally quiescent state until needed (13). In addition, *Drosophila* Nanos promotes the deadenylation of poly(A) tail in *hunchback* mRNA and represses its translation without changing the mRNA level

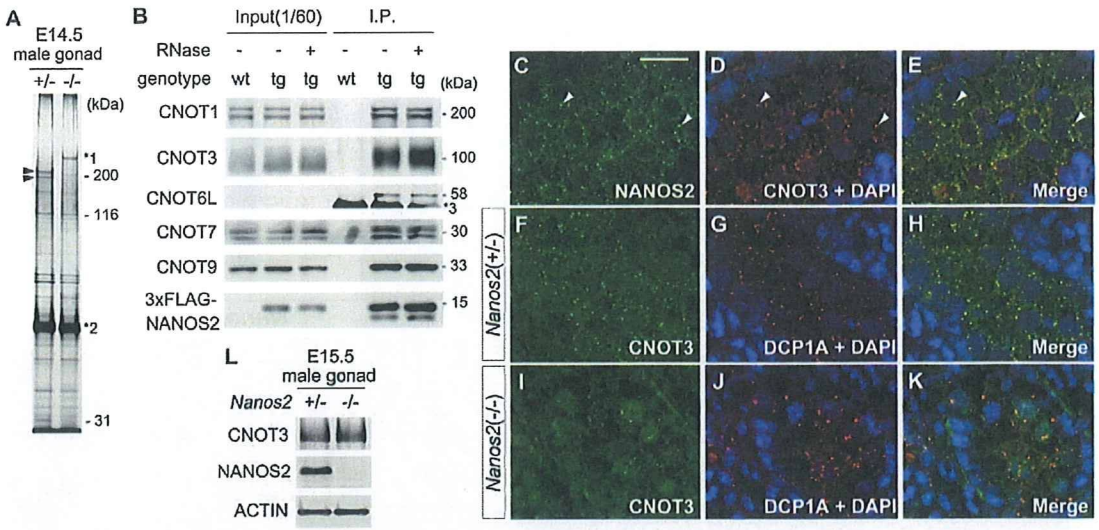

Fig. 3. Interaction between NANOS2 and the CCR4-NOT deadenylation complex. (*A*) Proteins coimmunoprecipitated with NANOS2 from E14.5 wild-type (lane 1) and *Nanos2*$^{-/-}$ (lane 2) male gonadal extracts using rabbit anti-NANOS2 antibodies. Arrowheads indicate CNOT1. *1, nonspecific band; *2, IgG polypeptide. (*B*) Immunoprecipitation–Western blot analyses of proteins from male gonadal extracts of wild-type and transgenic embryos expressing 3xFLAG-NANOS2. *3, IgG polypeptide from the anti-FLAG antibody. (*C–E*) Male gonadal sections from E15.5 embryos were immunostained with mouse NANOS2 (green) (*C*) and CNOT3 (red) (*D*) antibodies. Arrowheads in *C–E* indicate colocalization between NANOS2 and CNOT3. (*F–K*) Male gonadal sections from *Nanos2*$^{+/-}$ (*F–H*) and *Nanos2*$^{-/-}$ (*I–K*) embryos at E15.5 were immunostained with DCP1A (red) (*G* and *J*) and CNOT3 (green) (*F* and *I*) antibodies. DNA was labeled via DAPI counterstaining (blue). (*L*) Western blot analyses of proteins from the male gonads of *Nanos2*$^{+/-}$ and *Nanos2*$^{-/-}$ embryos at E15.5.

(34). We cannot therefore rule out the possibility that NANOS2 not only promotes the degradation of mRNAs involved in meiosis but also retains other transcripts at P-bodies to sequester them in a translationally inactive state during embryogenesis. These transcripts may be released from the P-bodies and translated to promote differentiation after birth as NANOS2 expression begins to disappear.

P-Body Formation in Male Mouse Gonocytes. P-bodies have been well characterized in yeast and mammalian cultured cells, and the in vivo status of these foci has begun to be described recently also in worms and flies (35–38). We found from our current analyses that P-bodies are specifically formed and/or maintained in the germ cells of male mouse embryonic gonads, whereas no such structures are detectable in somatic cells. Furthermore, female mouse gonocytes fail to maintain P-bodies at later stages of embryogenesis. We thus suggest that P-bodies play roles in cell-type specific differentiation during mouse development through RNA metabolism.

It has also been shown that P-bodies are dynamic structures and that their size and number reflects the status of the mRNA supply. If the transit of mRNAs into the P-bodies is inefficient, the size and number of these structures becomes extremely small. In contrast, they become larger when the mRNA decapping pathway is blocked (39, 40). Furthermore, it has been recently reported that deadenylation is required for P-body formation (41). Taking into account the data presented in these earlier reports and our current model, P-bodies would be expected to be small in *Nanos2*$^{-/-}$ male gonocytes because the mRNA supply to these structures and subsequent deadenylation efficiency would be inhibited in the absence of NANOS2. However, we were surprised to find that the sizes of the P-bodies

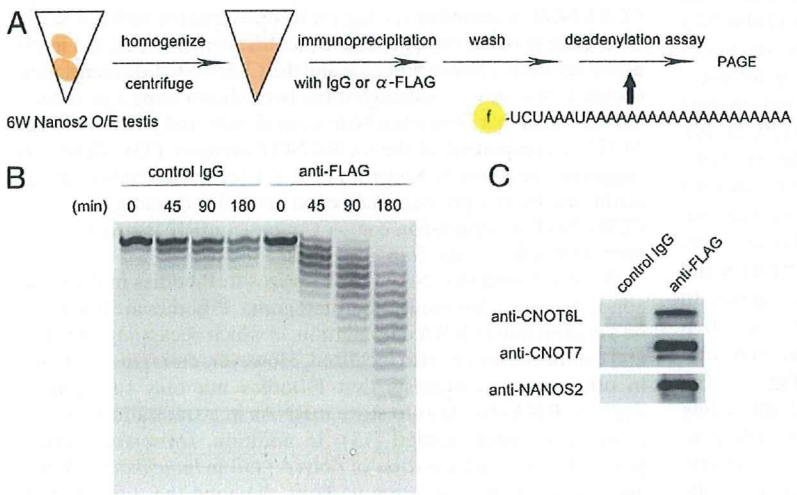

Fig. 4. The protein complex of NANOS2 and CCR4-NOT complex has in vitro deadenylase activity. (*A*) Schematic representation of the in vitro deadenylase assay method using NANOS2 over-expressing (O/E) testes. (*B*) FLAG-tagged NANOS2 was precipitated with anti-FLAG antibodies from the testis extracts of a 6-week-old NANOS2 O/E mouse and incubated with 5′-fluorescein isothiocyanate-labeled poly (A) RNA substrate for 0, 45, 90, and 180 min. Samples were then analyzed on a denaturing sequencing gel, as previously described (21) (*G*). (*C*) Western blot analyses reveaing that CNOT6L and CNOT7 are coprecipitated with FLAG-tagged NANOS2.

DEVELOPMENTAL BIOLOGY

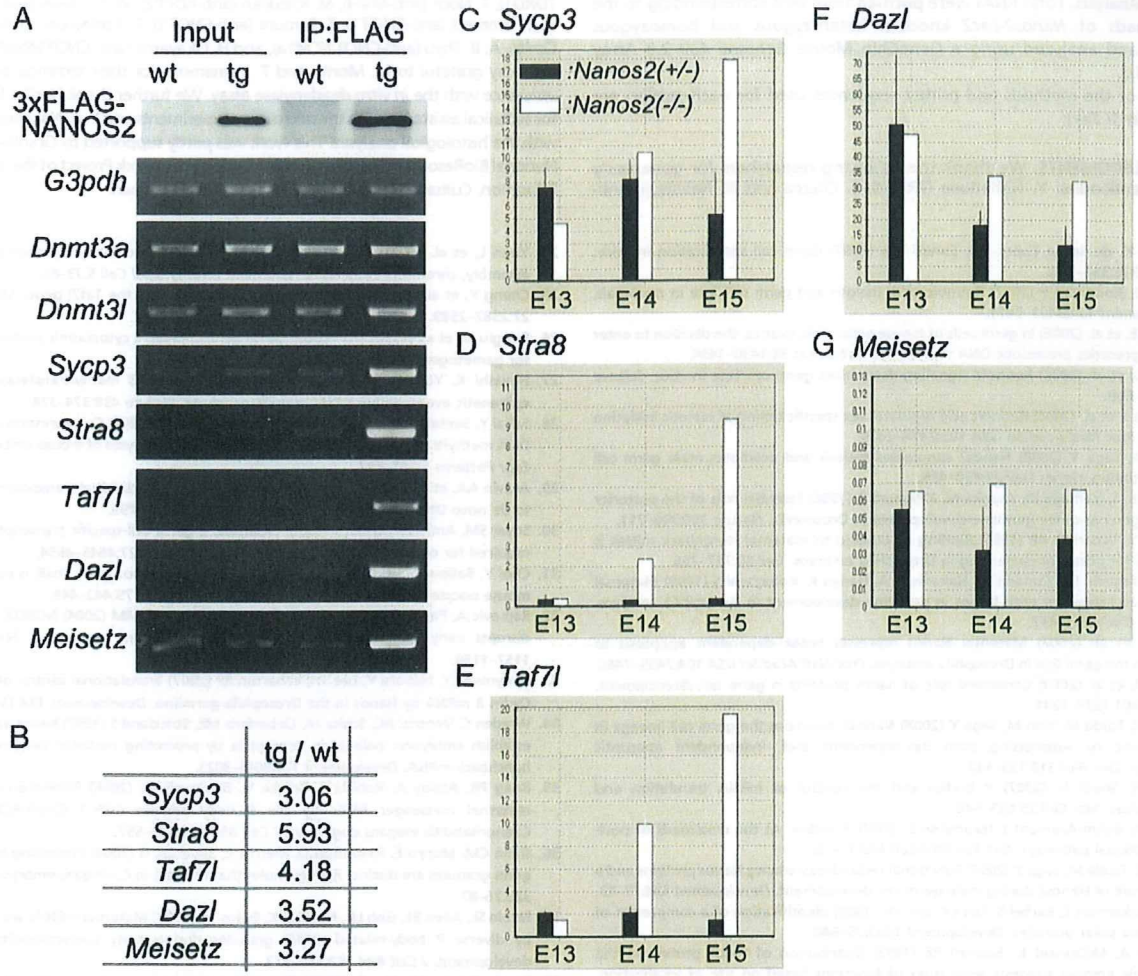

B

	tg / wt
Sycp3	3.06
Stra8	5.93
Taf7l	4.18
Dazl	3.52
Meisetz	3.27

Fig. 5. NANOS2 interacts with specific mRNAs and may promote their degradation. (*A*) Male gonadal extracts from wild-type (*wt*) and transgenic (*tg*) mice expressing FLAG-NANOS2 at E15.5 were subjected to immunoprecipitation (IP) with FLAG antibodies. RNA precipitates were analyzed by semi-quantitative RT-PCR. (*B*) Quantification of each mRNA enrichment from a FLAG IP of *tg* extracts using real-time RT-PCR. Fold enrichment of each mRNA coprecipitated from *tg* compared with those from *wt* is indicated. Mean value of three independent QRT-PCR results is shown. (*C–G*) Expression profiling of the *Sycp3* (*C*), *Stra8* (*D*), *Taf7l* (*E*), *Dazl* (*F*), and *Meisetz* (*G*) genes in male gonads from *Nanos2*$^{+/-}$ and *Nanos2*$^{-/-}$ embryos at E13.5-E15.5 using the Affymetrix GeneChip System as previously described (43) (*X*-axis; embryonic stage, *Y*-axis; expression level, black bars; *Nanos2*$^{+/-}$ embryos, white bars; *Nanos2*$^{-/-}$ embryos).

became larger in this biological context, although their number was decreased. These data thus indicate that male gonocytes have a unique program for P-body formation that occurs both in a NANOS2-dependent and -independent manner.

mRNAs Targeted by NANOS2. We elucidated that the protein complex of NANOS2 and CCR4-NOT complex has deadenylase activity in vitro. We thus expected that the poly(A) tail lengths of NANOS2-interacting mRNAs would be maintained without NANOS2. To test this scenario, we assayed the poly(A) tail length of NANOS2-interacting mRNAs. However, we could not observe clear shortening of the poly(A) tail in wild-type male gonads, possibly because of their low abundance. New experimental systems will be required in the future to address this issue.

On the other hand, it was noteworthy that we identified *Stra8* as a NANOS2-interacting mRNA because we have shown previously that *Stra8* is up-regulated at the transcriptional level in *Nanos2*$^{-/-}$ male gonocytes (6). These data together indicate that the suppression of *Stra8* in male gonocytes is ensured at both the transcriptional and translational levels, suggesting the critical functional importance of suppressing this gene during male gonocyte development.

Materials and Methods

Mice. Both the *Nanos2* and *Bax*-knockout mouse lines and PCR methods used for the verification of each mutant allele have been previously described (11, 42). The NANOS2-expressing mouse line has also been described (23) The transgene containing 3xFLAG-tagged *Nanos2* with the 3′-UTR under the control of Nanos2 enhancer (9.2 kb upstream sequence) was used for the production of the transgenic mouse line.

Histological Methods. For immunostaining, mouse gonads of both sexes were directly embedded in O.C.T. compound (Sakura) and frozen in liquid nitrogen. After sectioning (8 μm), samples were stained according to standard procedures.

Immunoprecipitation. Extracts of male gonads from E14.5 or E15.5 embryos were incubated with protein-A beads crosslinked with rabbit anti-NANOS2 antibody or anti-FLAG M2 affinity gel (Sigma).

In Vitro Deadenylase Assay. The testis extracts from NANOS2-expressing mice were incubated with anti-FLAG M2 affinity gel or Mouse IgG-agarose (Sigma). After several washes, precipitates were then subjected to a deadenylase assay as previously described (21).

RT-PCR. After synthesis of first-strand cDNAs with SuperScript III reverse transcriptase and $(dT)_{20}$ primer (Invitrogen), PCR analyses were carried out either using a regular or real-time protocol.

GeneChip Analysis. Total RNAs were purified from cells corresponding to the male gonads of *Nanos2-LacZ* knock-in heterozygous and homozygous embryos, and analyzed using a GeneChip Mouse Genome 430 2.0 Array (Affymetrix).

Details of the methods and primer sequences used for each section are provided in *SI Text*.

ACKNOWLEDGMENTS. We thank the following researchers for generously providing antibodies: Y. Nishimune (TRA98), S. Chuma and N. Nakatsuji (anti-TDRD1), T. Noce (anti-MVH), M. Kiledjian (anti-hDCP2), W. D. Heyer (anti-mXRN1), H. T. Timmers (anti-CNOT1), T. Tamura (anti-CNOT3), T. Yamamoto (anti-CNOT6L/Ccr4b), A. B. Shyu (anti-CNOT7/Caf1a), and H. Okayama (anti-CNOT9/Rcd1). We are also very grateful to M. Morita and T. Yamamoto for their technical advice and assistance with the *in vitro* deadenylase assay. We further thank Noriko Moriyama for technical assistance with the microarray experiments and Yuki Nakajima for help with the histological analyses. This work was partly supported by Grants-in-Aid for National BioResource Project and of the Genome Network Project of the Ministry of Education, Culture, Sports, Science and Technology, Japan.

1. Hayashi K, de Sousa Lopes SM, Surani MA (2007) Germ cell specification in mice. *Science* 316:394–396.
2. Bowles J, Koopman P (2007) Retinoic acid, meiosis and germ cell fate in mammals. *Development* 134:3401–3411.
3. Baltus AE, et al. (2006) In germ cells of mouse embryonic ovaries, the decision to enter meiosis precedes premeiotic DNA replication. *Nat Genet* 38:1430–1434.
4. Bowles J, et al. (2006) Retinoid signaling determines germ cell fate in mice. *Science* 312:596–600.
5. Koubova J, et al. (2006) Retinoic acid regulates sex-specific timing of meiotic initiation in mice. *Proc Natl Acad Sci USA* 103:2474–2479.
6. Suzuki A, Saga Y (2008) Nanos2 suppresses meiosis and promotes male germ cell differentiation. *Genes Dev* 22:430–435.
7. Kobayashi S, Yamada M, Asaoka M, Kitamura T (1996) Essential role of the posterior morphogen nanos for germline development in Drosophila. *Nature* 380:708–711.
8. Murata Y, Wharton RP (1995) Binding of pumilio to maternal hunchback mRNA is required for posterior patterning in Drosophila embryos. *Cell* 80:747–756.
9. Asaoka-Taguchi M, Yamada M, Nakamura A, Hanyu K, Kobayashi S (1999) Maternal Pumilio acts together with Nanos in germline development in Drosophila embryos. *Nat Cell Biol* 1:431–437.
10. Sato K, et al. (2007) Maternal Nanos represses hid/skl-dependent apoptosis to maintain the germ line in Drosophila embryos. *Proc Natl Acad Sci USA* 104:7455–7460.
11. Tsuda M, et al. (2003) Conserved role of nanos proteins in germ cell development. *Science* 301:1239–1241.
12. Suzuki H, Tsuda M, Kiso M, Saga Y (2008) Nanos3 maintains the germ cell lineage in the mouse by suppressing both Bax-dependent and -independent apoptotic pathways. *Dev Biol* 318:133–142.
13. Parker R, Sheth U (2007) P bodies and the control of mRNA translation and degradation. *Mol Cell* 25:635–646.
14. Eulalio A, Behm-Ansmant I, Izaurralde E (2007) P bodies: At the crossroads of post-transcriptional pathways. *Nat Rev Mol Cell Biol* 8:9–22.
15. Suzuki A, Tsuda M, Saga Y (2007) Functional redundancy among Nanos proteins and a distinct role of Nanos2 during male germ cell development. *Development* 134:77–83.
16. Hay B, Ackerman L, Barbel S, Jan LY, Jan YN (1988) Identification of a component of Drosophila polar granules. *Development* 103:625–640.
17. Bardsley A, McDonald K, Boswell RE (1993) Distribution of tudor protein in the Drosophila embryo suggests separation of functions based on site of localization. *Development* 119:207–219.
18. Toyooka Y, et al. (2000) Expression and intracellular localization of mouse Vasa-homologue protein during germ cell development. *Mech Dev* 93:139–149.
19. Chuma S, et al. (2003) Mouse Tudor Repeat-1 (MTR-1) is a novel component of chromatoid bodies/nuages in male germ cells and forms a complex with snRNPs. *Mech Dev* 120:979–990.
20. Kedersha N, Anderson P (2007) Mammalian stress granules and processing bodies. *Methods Enzymol* 431:61–81.
21. Morita M, et al. (2007) Depletion of mammalian CCR4b deadenylase triggers elevation of the p27Kip1 mRNA level and impairs cell growth. *Mol Cell Biol* 27: 4980–4990.
22. Meyer S, Temme C, Wahle E (2004) Messenger RNA turnover in eukaryotes: Pathways and enzymes. *Crit Rev Biochem Mol Biol* 39:197–216.
23. Sada A, Suzuki A, Suzuki H, Saga Y (2009) The RNA-binding protein NANOS2 is required to maintain murine spermatogonial stem cells. *Science* 325:1394–1398.
24. Yuan L, et al. (2000) The murine SCP3 gene is required for synaptonemal complex assembly, chromosome synapsis, and male fertility. *Mol Cell* 5:73–83.
25. Cheng Y, et al. (2007) Abnormal sperm in mice lacking the Taf7l gene. *Mol Cell Biol* 27:2582–2589.
26. Ruggiu M, et al. (1997) The mouse Dazla gene encodes a cytoplasmic protein essential for gametogenesis. *Nature* 389:73–77.
27. Hayashi K, Yoshida K, Matsui Y (2005) A histone H3 methyltransferase controls epigenetic events required for meiotic prophase. *Nature* 438:374–378.
28. Sakai Y, Suetake I, Shinozaki F, Yamashina S, Tajima S (2004) Co-expression of de novo DNA methyltransferases Dnmt3a2 and Dnmt3L in gonocytes of mouse embryos. *Gene Expr Patterns* 5:231–237.
29. Aravin AA, et al. (2008) A piRNA pathway primed by individual transposons is linked to de novo DNA methylation in mice. *Mol Cell* 31:785–799.
30. Soyal SM, Amleh A, Dean J (2000) FIGalpha, a germ cell-specific transcription factor required for ovarian follicle formation. *Development* 127:4645–4654.
31. Choi Y, Ballow DJ, Xin Y, Rajkovic A (2008) Lim homeobox gene, lhx8, is essential for mouse oocyte differentiation and survival. *Biol Reprod* 79:442–449.
32. Rajkovic A, Pangas SA, Ballow D, Suzumori N, Matzuk MM (2004) NOBOX deficiency disrupts early folliculogenesis and oocyte-specific gene expression. *Science* 305: 1157–1159.
33. Kadyrova LY, Habara Y, Lee TH, Wharton RP (2007) Translational control of maternal Cyclin B mRNA by Nanos in the Drosophila germline. *Development* 134:1519–1527.
34. Wreden C, Verrotti AC, Schisa JA, Lieberfarb ME, Strickland S (1997) Nanos and pumilio establish embryonic polarity in Drosophila by promoting posterior deadenylation of hunchback mRNA. *Development* 124:3015–3023.
35. Boag PR, Atalay A, Robida S, Reinke V, Blackwell TK (2008) Protection of specific maternal messenger RNAs by the P body protein CGH-1 (Dhh1/RCK) during Caenorhabditis elegans oogenesis. *J Cell Biol* 182:543–557.
36. Gallo CM, Munro E, Rasoloson D, Merritt C, Seydoux G (2008) Processing bodies and germ granules are distinct RNA granules that interact in C. elegans embryos. *Dev Biol* 323:76–87.
37. Noble SL, Allen BL, Goh LK, Nordick K, Evans TC (2008) Maternal mRNAs are regulated by diverse P body-related mRNP granules during early Caenorhabditis elegans development. *J Cell Biol* 182:559–572.
38. Lee L, Davies SE, Liu JL (2009) The spinal muscular atrophy protein SMN affects Drosophila germline nuclear organization through the U body-P body pathway. *Dev Biol* 332:142–155.
39. Sheth U, Parker R (2003) Decapping and decay of messenger RNA occur in cytoplasmic processing bodies. *Science* 300:805–808.
40. Eulalio A, Behm-Ansmant I, Schweizer D, Izaurralde E (2007) P-body formation is a consequence, not the cause, of RNA-mediated gene silencing. *Mol Cell Biol* 27: 3970–3981.
41. Zheng D, et al. (2008) Deadenylation is prerequisite for P-body formation and mRNA decay in mammalian cells. *J Cell Biol* 182:89–101.
42. Knudson CM, Tung KS, Tourtellotte WG, Brown GA, Korsmeyer SJ (1995) Bax-deficient mice with lymphoid hyperplasia and male germ cell death. *Science* 270: 96–99.
43. Kanno J, et al. (2006) "Per cell" normalization method for mRNA measurement by quantitative PCR and microarrays. *BMC Genomics* 7:64.

OPEN ACCESS Freely available online PLoS COMPUTATIONAL BIOLOGY

Structure of Protein Interaction Networks and Their Implications on Drug Design

Takeshi Hase[1☯], Hiroshi Tanaka[2☯*], Yasuhiro Suzuki[3], So Nakagawa[4], Hiroaki Kitano[5,6,7*]

1 Department of Bioinformatics, Medical Research Institute, Tokyo Medical and Dental University, Bunkyo-ku, Tokyo, Japan, **2** Department of Bioinformatics, Graduate School of Biomedical Science, Tokyo Medical and Dental University, Bunkyo-ku, Tokyo, Japan, **3** Department of Complex Systems Science, Graduate School of Information Science, Nagoya University, Nagoya, Aichi, Japan, **4** Center for Information Biology and DNA Databank of Japan, National Institute of Genetics, Mishima, Shizuoka, Japan, **5** Sony Computer Science Laboratories, Shinagawa, Tokyo, Japan, **6** The Systems Biology Institute, Minato, Tokyo, Japan, **7** Okinawa Institute of Science and Technology, Kunigami, Okinawa, Japan

Abstract

Protein-protein interaction networks (PINs) are rich sources of information that enable the network properties of biological systems to be understood. A study of the topological and statistical properties of budding yeast and human PINs revealed that they are scale-rich and configured as highly optimized tolerance (HOT) networks that are similar to the router-level topology of the Internet. This is different from claims that such networks are scale-free and configured through simple preferential-attachment processes. Further analysis revealed that there are extensive interconnections among middle-degree nodes that form the backbone of the networks. Degree distributions of essential genes, synthetic lethal genes, synthetic sick genes, and human drug-target genes indicate that there are advantageous drug targets among nodes with middle- to low-degree nodes. Such network properties provide the rationale for combinatorial drugs that target less prominent nodes to increase synergetic efficacy and create fewer side effects.

Citation: Hase T, Tanaka H, Suzuki Y, Nakagawa S, Kitano H (2009) Structure of Protein Interaction Networks and Their Implications on Drug Design. PLoS Comput Biol 5(10): e1000550. doi:10.1371/journal.pcbi.1000550

Editor: Andrey Rzhetsky, University of Chicago, United States of America

Received June 22, 2009; **Accepted** September 29, 2009; **Published** October 30, 2009

Funding: A part of this research is supported by Japan Science and Technology Agency (JST) through ERATO-SORST Program to HK. The funders had no role in study design, data collection and analysis, decision to publish, or preparation of the manuscript.

Competing Interests: The authors have declared that no competing interests exist.

* E-mail: kitano@sbi.jp (HK); tanaka@cim.tmd.ac.jp (HT)

☯ These two authors contributed equally to the article.

Introduction

There is a growing awareness that networks of protein interactions and gene regulations are the keys to understanding diseases and finding accurate drug targets [1]. With the increasing availability of genome-wide data including those on protein interactions and gene expressions, numbers of studies have been done on the structure and statistics of protein interactions and how diseased genes and drug targets are distributed over the network [2,3]. Understanding the topological and statistical properties of interaction networks and their relationships with lethal genes as well as currently identified drug targets should provide us with insights into robust and fragile properties of networks and possible drug targets for the future. We studied budding-yeast and human protein-protein interaction networks (PINs) to identify the architectural properties of network structures.

PINs have often been argued to be "scale-free" [4,5], which mostly means they have power-law frequency-degree distributions. However, this definition diverges from the original meaning of being scale-free in terms of the self-similarity of geometric properties of subject systems and there have been reports that claim such distributions are "more normal than normal"; thus, they are not considered to be particularly exotic by themselves [6]. In addition, there are different network topologies with different robustness and performance properties that maintain power-law distributions [7]. Therefore, it is very important to identify the architectural features of the network bearing the specific utilization of analysis results in mind. Our goal in this study was to identify the network topology of PINs and their relationship with lethal genes and possible drug targets so that the statistical likelihood of novel drug targets could be inferred.

A particularly interesting issue in the field of systems engineering, physics, and systems biology is the trade-off between the properties of robustness, fragility, and efficiency. Highly optimized tolerance (HOT) theory is a conceptual framework that can be used to explain this issue. Although a system conforming to HOT theory is optimized for specific perturbations and has highly efficient properties, such a system is extremely fragile against unexpected perturbations [8,9]. Doyle et al. [8] demonstrated that the Abline Internet2 router-level topology network conformed to HOT theory. Nodes in the Abline network with extremely high-degree nodes connect to a large number of low-degree nodes, while links between these high-degree nodes are suppressed and thus they do not form a core backbone for the whole network. A network having similar structures to the Abline network is defined as a HOTnet [8]. It would be very interesting to clarify whether PINs are HOTnets or not.

The two questions addressed in this paper are: (1) what is the global architecture of PINs? Do they follow the possible architectural features of scale-free networks created by preferential attachments or conform to HOT theory, and (2) are there specific statistical features for proteins that are likely to be drug targets? To

Author Summary

Genome-wide data on interactions between proteins are now available, and networks of protein interactions are the keys to understanding diseases and finding accurate drug targets. This study revealed that the architectural properties of the backbones of protein interaction networks (PINs) were similar to those of the Internet router-level topology by using statistical analyses of genome-wide budding yeast and human PINs. This type of network is known as a highly optimized tolerance (HOT) network that is robust against failures in its components and that ensures high levels of communication. Moreover, we also found that a large number of the most successful drug-target proteins are on the backbone of the human PIN. We made a list of proteins on the backbone of the human PIN, which may help drug companies to search more efficiently for new drug targets.

answer these questions, budding yeast and human PINs were used to analyze their structural properties using a series of analysis methods.

Results

Scale-free Network vs. Highly Optimized Tolerance Network: A series of analyses was carried out using budding yeast and human PIN data to identify the topological features of PINs.

In this study, we defined low-degree nodes as nodes with degrees of less than 5 because Han et al. [10] and Partil and Nakamura [11] defined hubs as nodes with degrees of more than 6. We then developed a method called moving stratification by degrees (MSD) to extract sub-networks consisting of hubs with specific degree distributions where indices such as average cluster coefficients would be computed (see Materials and Methods for details). The analyses revealed that the average cluster coefficient was very high for sub-networks consisting of hubs with degrees from 6 to 38, while it was very low for hubs with degrees of more than 39 in the yeast PIN (see Figure S1 and Table S1). Notably, for hubs with degrees of less than 38, the difference in cluster coefficients was generally significant between the yeast PIN and random network, while there were no significant differences in cluster coefficients for hubs with degrees of more than 39 (see Figure S1). Therefore, we defined middle-degree nodes as those with degrees from 6 to 38 and those with degrees of more than 39 as high. In the same manner, we defined middle- (from 6 to 30) and high-degree (more than 31) nodes in the human PIN (see Figure S2 and Table S2). Note that, when we used more stringent thresholds for middle- (from 10 to 50) and high-degree (more than 51) nodes, the results did not change essentially, i.e., the average cluster coefficient for middle-degree nodes was much higher than that for high-degree nodes (see Tables S3 and S4).

The analyses revealed three findings: (1) the network structure for middle-degree nodes (from 6 to 38 for yeast and from 6 to 30 for human PINs), and high-degree nodes (more than 39 for yeast and more than 31 for human PINs) has different structures, (2) middle-degree nodes are tightly connected and form a structure often called a "stratus", and (3) high-degree nodes do not connect, but connect with low-degree nodes, and form an "altocumulus" structure (Figures 1 and 2). Notably, we used more stringent thresholds for middle- (degrees from 10 to 50) and high-degree nodes (degrees more than 51), and found that changing the thresholds did not essentially affect the results (see Figure S3 and S4). These results suggests that PINs have an architecture where highly interconnected middle-degree nodes form a core backbone for the whole network and large numbers of low-degree nodes connect to high-degree nodes (see Figure 2). This architecture is a type of network that is suggested as a HOTnet, i.e., a network with HOT properties, also seen in the Internet router-level topology [8]. To further confirm this observation, we calculated a graph-theoretic quantity, $s(g)$, that defines the likelihood high-degree nodes will be connected to one another (see Materials and Methods for details). $S(g)$, a value normalized against s_{max}, indicates that networks with tightly interconnected high-degree nodes tend to be closer to 1.0, whereas networks with only sparsely interconnected high-degree nodes tend to be closer to 0.0 (see Materials and Methods for details). Doyle et al. reported randomly generated preferential-attachment-type scale-free networks had relatively high values such as 0.61, whereas a HOTnet exemplified by a network abstracted from an actual Abilene Internet2 router topology network had a value as low as 0.34 [8]. We found that the value of $S(g)$ for the yeast PIN was 0.25 and that of the human PIN was 0.38. Thus, we could conclude that PINs are HOTnets.

PINs are networks with a modular structure [12–14]. Here, modularity is defined as characteristics where there are fewer links

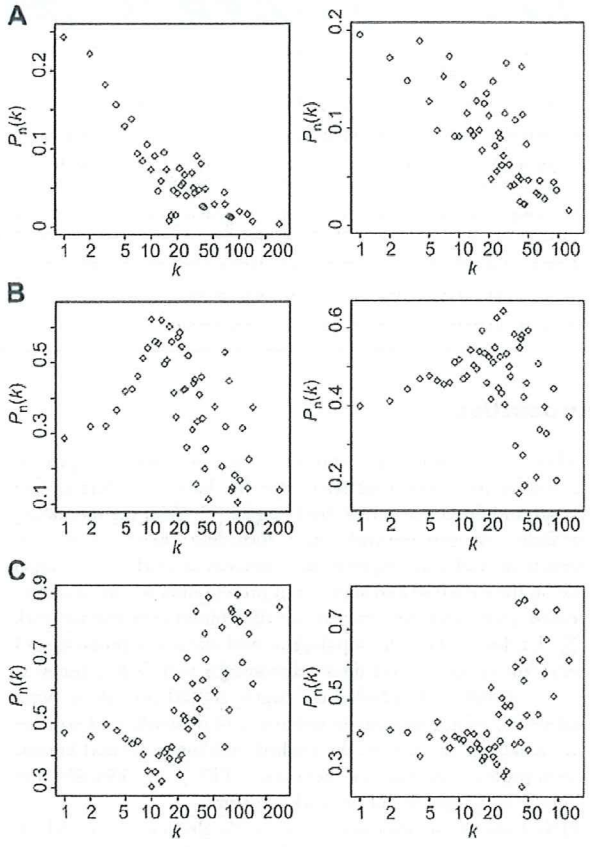

Figure 1. Degree dependent connectivity chart. $P_n(k)$ gives the probability that a link of a k-degree node is a link to a node in each sub-network of the yeast (left) and human (right) PINs. The value of $P_n(k)$ is calculated for a sub-network consisting of high-degree nodes, that consisting of middle-degree nodes, and that consisting of low-degree nodes. **(A)** Distribution of $P_n(k)$ for the high-degree sub-network. **(B)** Distribution of $P_n(k)$ for the middle-degree sub-network. **(C)** Distribution of $P_n(k)$ for the low-degree sub-network.
doi:10.1371/journal.pcbi.1000550.g001

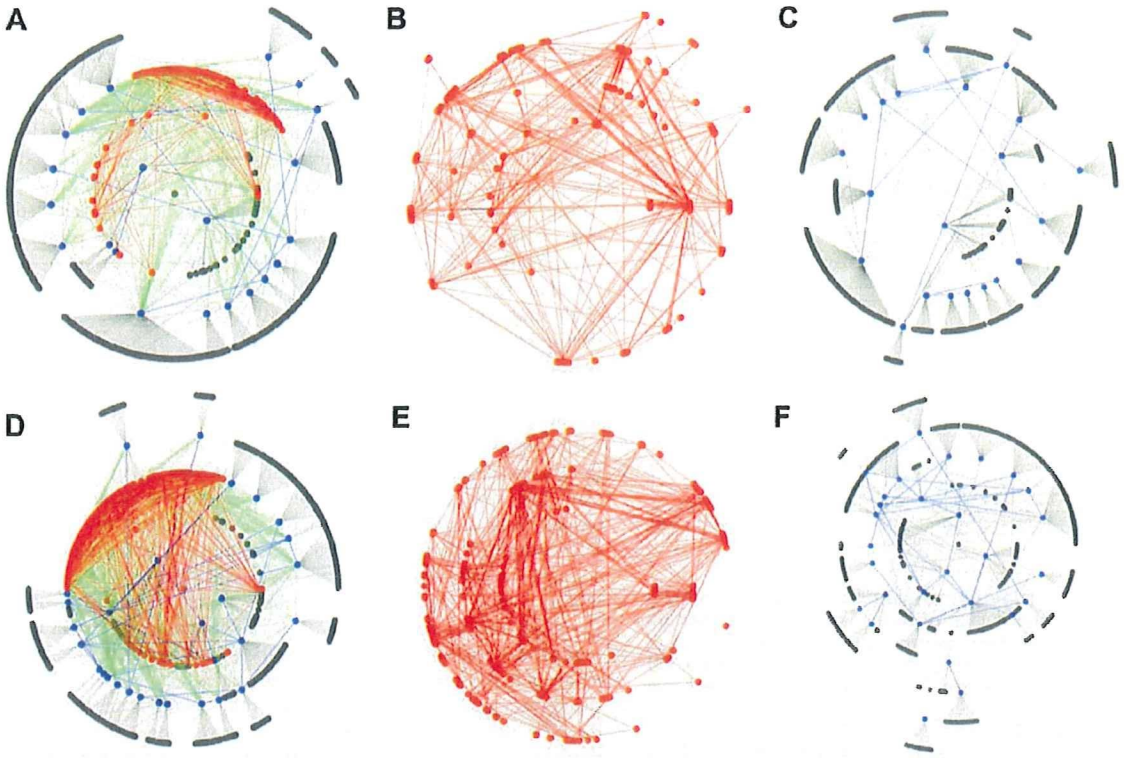

Figure 2. Cloud topology in yeast and human PINs. Grey, red, and blue nodes correspond to low-, middle-, and high-degree nodes. Grey, red, green, and blue links correspond to links between low- and high-degree nodes, those between middle-degree nodes, those between middle- and high-degree nodes, and those between high-degree nodes. For clarity, low- and middle-degree nodes that have no links to high-degree nodes have been omitted. **(A)** Altocumulus and stratus structures in the yeast PIN. **(B)** Stratus structure in the yeast PIN. **(C)** Altocumulus structure in the yeast PIN. **(D)** Altocumulus and stratus structure in the human PIN. **(E)** Stratus structure in the human PIN. **(F)** Altocumulus structure in the human PIN.
doi:10.1371/journal.pcbi.1000550.g002

between nodes with similar degrees. This only means there are limited links between high-degree nodes (hubs), whereas there are links between hubs and low-degree nodes. This is a feature that was also confirmed in this study (see Figure 2). Modularity in PINs implies that networks have two features [13]: First, functional units may be composed of many low-degree nodes that are directly connected to a hub node. Second, confusion between modules is avoided by avoiding direct connection between hubs. While there are arguments against this claim that hubs are tightly connected because they need to influence one another to achieve an integrated function for the whole system [15], analysis results indicate that such integration is most likely to take place via middle-degree nodes instead of high-degree nodes (see Figure 2).

The distribution of essential genes, synthetic genes, and other genes are shown in Figure 3. It is interesting to note that both essential genes and synthetic lethal genes have similar distributions. The average degree of essential proteins is 4.95 and that of synthetic lethal proteins is 4.40. However, the Wilcoxon rank sum test demonstrated that there is no statistical significance between them ($P = 0.334$). In either case, essential and synthetic lethal proteins are concentrated on middle-degree nodes and high-degree nodes. However, the average degree among synthetic sick genes is 4.07 and this is significantly lower than that among synthetic lethal genes ($P = 0.0015$). This means genes that have less severe impact are distributed toward regions with a lower-degree distribution.

Scale-richness: The power law distribution often characterized for scale-free networks only means that local frequency-degree distributions are independent of location along the degree axis, rather than self-similarity of network structures. However, Tanaka demonstrated that bacterial metabolic networks are scale rich in the sense there are different categories of metabolites and enzymes depending on the degree of nodes [16]. A group of nodes with high degree tends to be composed of currency molecules such as ATP and a group of nodes with low degree mostly consists of enzymes involved in specific cellular functions. In this study, we investigated if the frequency-degree distribution of proteins for each functional category exhibited the scale-rich characteristics reported by Tanaka. Figures 4 and S5 correspond to frequency-degree plots for proteins in different functional categories in the yeast PIN and the human PIN. The functional categories were assigned based on the GO slim ontology. As shown in the figures, the degree distribution patterns differ among functional categories. Moreover, proteins with different GO slim annotations have different average degrees (See Tables S5 and S6). Note that many functional categories have significantly higher (or lower) average degrees than the whole PINs (See Tables S5 and S6). These results suggest that the yeast and human PINs are scale-rich.

Drug Targets: Drug-target molecules are distributed over low- to middle-level degree nodes with higher probability on middle-degree nodes. Consistent with reports already published, the average degree among drug-target nodes (4.74) is higher than the average degree among all nodes (4.06).

The distribution of known drug targets is shown in Figure 5 and this is predominantly distributed to middle-degree nodes and

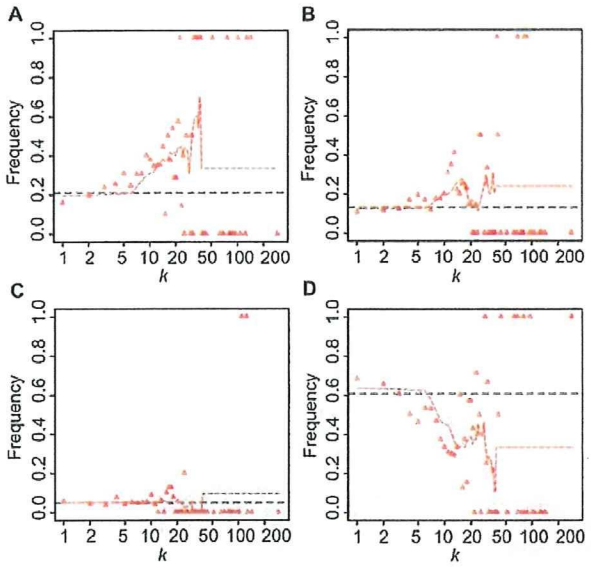

Figure 3. Degree distribution of essential proteins, synthetic lethal proteins, synthetic sick proteins, and proteins that do not belong to any of these (normal proteins). (A) Fraction of essential proteins to all proteins with degree k (red triangles). **(B)** Fraction of synthetic lethal proteins to all proteins with degree k (red triangles). **(C)** Fraction of synthetic sick proteins to all proteins with degree k (red triangles). **(D)** Fraction of normal proteins to all proteins with degree k (red triangles). Dashed lines in black give the probability that a randomly selected protein is essential, synthetic lethal, synthetic sick, or normal. Dashed lines in red represent fraction of essential, synthetic lethal, synthetic sick, or normal proteins to all proteins with degree from $k-5$ to $k+5$, when $k \leq 38$. When $k>38$, dashed lines in red represent fraction of essential, synthetic lethal, synthetic sick, or normal proteins to all proteins with degrees more than 38.
doi:10.1371/journal.pcbi.1000550.g003

mostly on backbone of the network. There are almost no drug targets for high-degree nodes. The distribution of drug targets for cancer and non-cancerous diseases are in sharp contrast. While the average degree of target nodes for cancer drugs was 7.82, the targets for non-cancerous diseases scored only 4.24 ($P=0.01$). Moreover, we found that the proportion of drug targets among low-degree proteins were similar to random expectation. Figure 6 shows distribution of drug targets marked on degree-rank plot. The drug target molecule that has highest degree is Src with 41 which is the target for drugs such as Dasatinib. Target molecules for anti-cancer drugs are shifted toward high degree nodes compare against average and non-anti-cancer drugs.

Discussion

A series of analyses revealed that both the budding yeast and human PINs are scale-rich and have HOT networks. There are extensive interconnections among middle-degree nodes that form the backbone of the network (see Figure 2). Most drug-target genes concentrate on middle-degree nodes and parts of low-degree nodes, but not on high-degree nodes. Interestingly, Feldman et al. (2008) [17] reported that genes harboring inherited disease mutations also concentrated on middle-degree nodes. Because of the potential lethality observed in budding yeast (Figure 3A) and reported high lethality in mouse knockout [2], high-degree nodes are unlikely to be preferred drug targets or genes with disease mutations. Since oncogenes tend to be high-degree nodes, they are less likely to be drug targets, or one has to accept major potential side effects. The fact that the degree distribution of cancer-drug targets is higher than that of non-cancer-drug targets is consistent with the report by Yao and Rzhetsky [18]. Since high-degree nodes are predominantly connected with low-degree nodes (Figures 1, 2, S3, and S4), the elimination of high-degree nodes is likely to affect large numbers of low-degree nodes. This may result in unacceptable side effects since a group of genes that bear certain functions may be made collectively dysfunctional. Detailed case studies are warranted to test and verify this possible interpretation. However, the average degree distribution of synthetic sick genes (4.07) is less than that of essential genes (4.95) and synthetic lethal genes (4.40). This implies that a drug design strategy to generate synergetic effects by targeting less important targets can be a reasonable option because each compound in such drugs can select targets that have less impact on the overall system alone.

We found that middle-level degree nodes are the optimal targets for therapeutic drugs. A similar observation was reported by Yao and Rzhetsky [18], although they measured the mean degree among drug targets. In this study, we investigated the degree distribution of drug targets in greater detail, because we measured a fraction of drug targets to all nodes with degree k as well as mapping drug targets on the network structure. It was clearly identified most of drug targets for drugs that are currently on the market are concentrated on middle degree nodes that are back bone of the network and low-degree nodes that tends to have specific function specific effects. One of novel findings here is that the distribution of drug targets for low-degree nodes is similar to random expectation, indicating that there are a certain number of low-degree drug targets. From these results, we can expect that the most advantageous targets for combinatorial drugs could be among low-degree nodes because these could have less severe impact on the overall system of the human body. This is consistent with the idea of "long-tail drugs" [19].

Are there any relationships between structures in molecular networks (i.e., scale-richness in PINs) and the properties of their underlying genome? Rzhetsky and Gomez [20] proposed a stochastic model describing the evolutionary growth of molecular networks. Their model predicts that, in a molecular network, the shape of the degree distribution will be similar to the shape of the distribution of domains in the genome. Actually, they showed that, in the case of the entire yeast PIN, both the degree distribution and the distribution of the domain followed a power law. Therefore, it might be interesting to see whether, for each functional category, the shape of the degree distribution was similar to that of the domain distribution, when the entire architecture of domains in genomes becomes available.

In this study, we assumed that the PINs represented all functions of genes. However, the PINs are just composed of binary protein-protein binding and proteins have other types of functions, such as catalyzing reactions with non-protein substrates. Therefore, PINs reflect a subset of the entire cellular function. This indicates that, if the complete picture for cellular protein functions could be considered, our conclusions from the PINs may diverge from what we presented here. Moreover, at present, the yeast and human PINs represent incomplete pictures of the actual entire PINs of these organisms. When data on all the actual entire PINs become available, we intend to examine all the actual entire PINs to see whether similar observations to those in this study can be made or not.

It is interesting to note that both PINs and the Internet topology are HOTnets. Many of the observed properties in Internet router topology may be applied to PINs as well. Such properties include

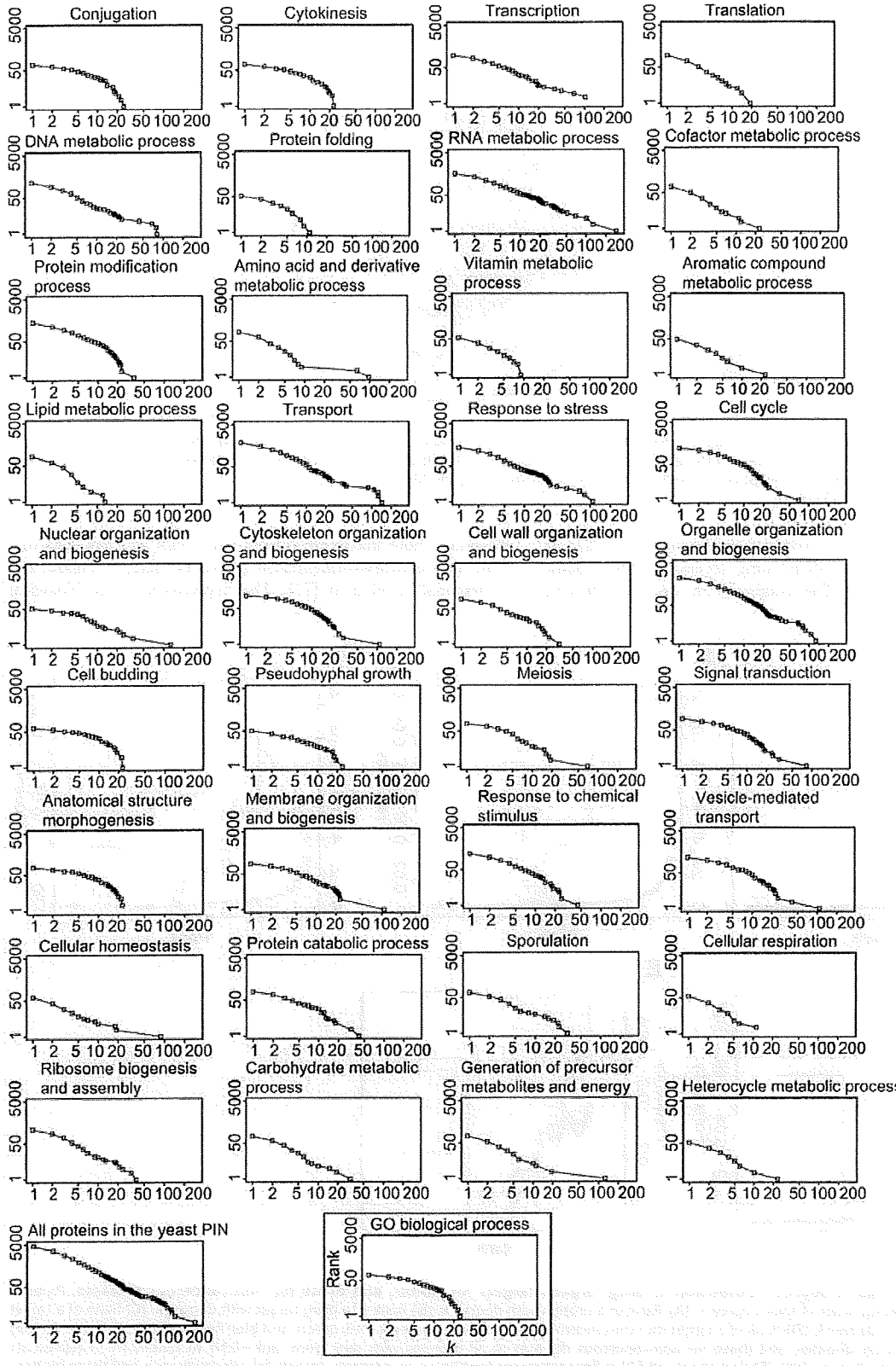

Figure 4. Scale-richness in yeast PIN. Each diagram shows cumulative degree distributions of proteins in each functional group. The name above each diagram denotes the name of the functional category with which the cumulative degree distribution was examined.
doi:10.1371/journal.pcbi.1000550.g004

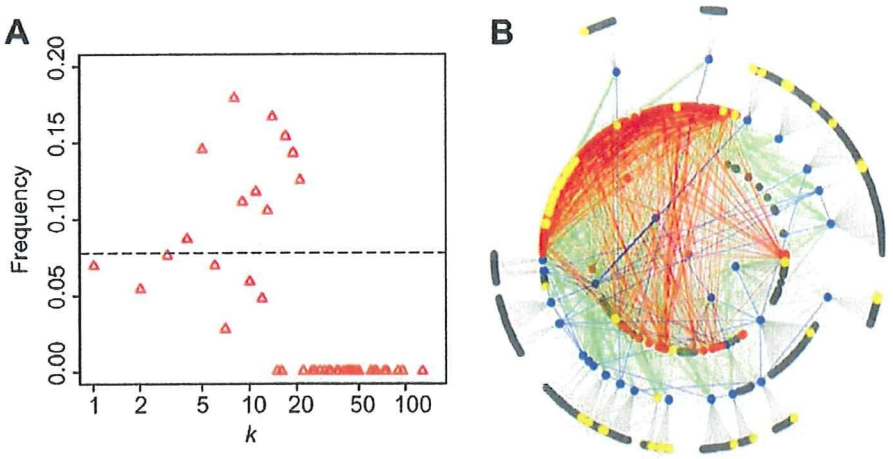

Figure 5. Distribution of drug targets. (A) Degree distribution. Red triangles represent fraction of drug-target proteins to all proteins with degree *k*. The dashed line in black gives the probability that a randomly selected protein is a drug target. **(B)** Distribution on network topology. Drugs targets (yellow circles) are mapped on human PIN network topology shown in Figure 2D.
doi:10.1371/journal.pcbi.1000550.g005

robustness against node failure and optimized performance [21]. It has been reported that analysis using several possible router topologies found that a HOTnet configuration was most efficient, providing more maximum overall bandwidth to users than that with other network-configuration approaches such as random and preferential attachment [21]. The implication is that biological

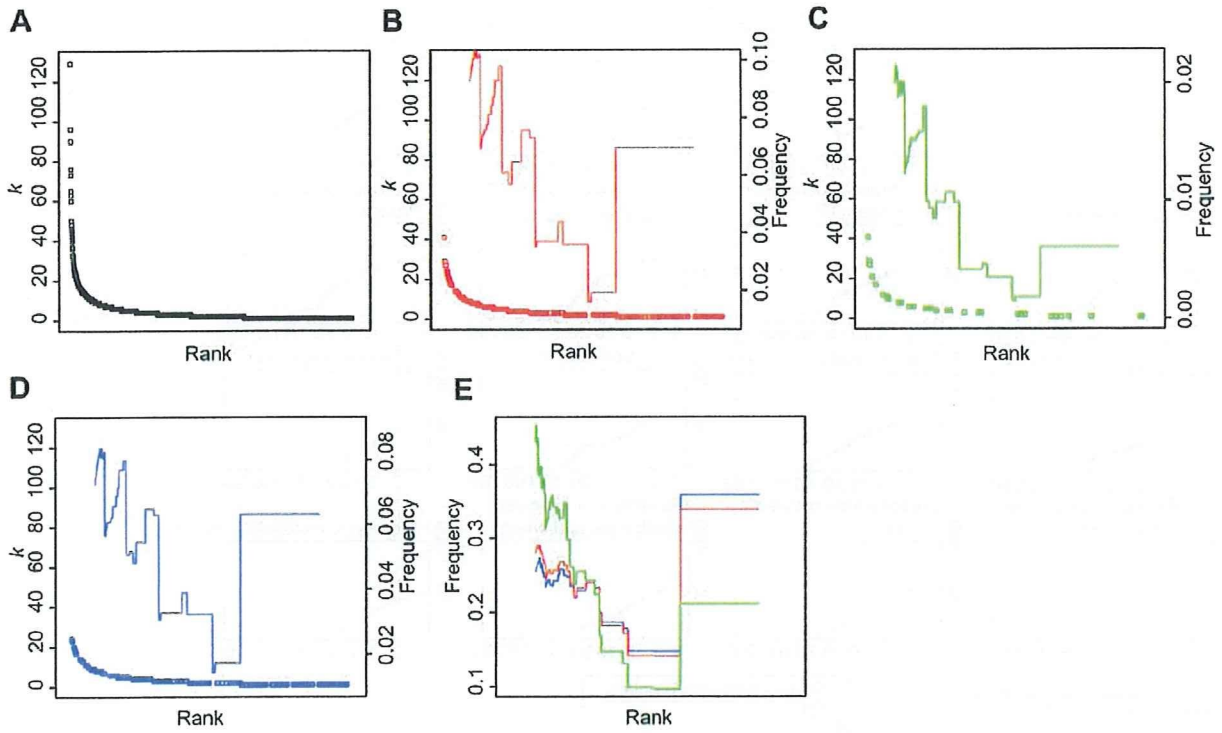

Figure 6. The long tails in degree distribution of drug targets, targets for cancer, and those for non-cancerous diseases. Proteins were ranked in decreasing order of their degree *k*. **(A)** Rank of a protein with degree *k*. **(B)** Rank of a drug target with degree *k*. **(C)** Rank of a target for cancer diseases with degree *k*. **(D)** Rank of a target for non-cancerous diseases with degree *k*. Red, green, and blue lines represent fraction of drug targets, targets for cancer diseases, and those for non-cancerous diseases to all proteins with rank from rank−0.1*N* to rank+0.1*N* (*N* represents number of proteins in the human PIN). **(E)** Red, green, and blue lines represent fraction of drug targets, targets for cancer disease, and those for non-cancerous disease with rank from rank−0.1*N* to rank+0.1*N* to all drug targets, all targets for cancer diseases, and those for non-cancerous diseases, respectively.
doi:10.1371/journal.pcbi.1000550.g006

PINs have evolved to become efficient and error tolerant. The series of analyses presented in this report indicate that there are changes whereby we can rationally design drugs by taking into account network properties, and additional insights from engineering and physics may further extend our opportunities for exploring network-based biology.

Materials and Methods

PINs, GO data, and essential genes. Yeast PIN data were obtained from the Munich Information Center for Protein Sequences (MIPS) database (http://mips.gsf.de) [22] and human PIN data were obtained from Rual et al. [23]. The yeast (or human) PIN contained 4,153 (or 3,023) proteins and 7,417 (or 6,149) non-redundant interactions. The GO slim dataset for the yeast PIN was from the ftp site of the Saccharomyces Genome Database (SGD) (ftp://genome-ftp.stanford.edu/pub/yeast/literature_curation/) [22] and that for the human PIN was from the European Bioinformatics Institute (EBI) (ftp://ftp.ebi.ac.uk/pub/databases/GO/goa/HUMAN/). The list of essential genes from SGD [22] contained 889 essential genes that were mapped to the yeast PIN.

Synthetic lethal and synthetic sick proteins. We obtained a list of synthetic lethal and sick interactions from Tong et al. [24]. There were 735 proteins having at least one synthetic lethal interaction and we defined these proteins as synthetic lethal proteins. However, there were 816 proteins having at least one synthetic sick interaction, of which 310 proteins had no synthetic lethal interactions. We defined these 310 proteins as synthetic sick proteins. 538 synthetic lethal proteins and 209 synthetic sick proteins were mapped to the yeast PIN.

Drug-target proteins. To analyze the statistical features of drug-target genes, we obtained a list of proteins that were targets of FDA-approved and experimental drugs from Yildirim et al. [3]. This list contained 1,013 drug-target proteins, of which 236 were mapped to the human PIN. To generate a list of drug-disease associations, we mapped drugs to diseases by investigating information on drugs obtained from the DrugBank database [25] (information on drugs is contained in the "indications" field in the DrugBank database). Then, by using the list of drug-disease associations, we divided drug-target proteins into two groups: target proteins for cancer drugs and those for non-cancerous diseases. The human PIN contained 33 target proteins for cancer and 203 for non-cancerous diseases.

Random network. We generated a random network by using the method proposed by Maslov and Sneppen [13], where the following procedures were performed. First, two links in a network were chosen randomly. Assume that one link connects nodes A and B, and the other connects nodes C and D. Second, these links were rewired by exchanging their connecting partners. That is, nodes A and D were connected, and nodes B and C were connected. We repeated these two procedures $1{,}000E$ times (E is the number of interactions in the original network) to generate a random network. Note that the method did not alter the degree distribution.

Cluster coefficient. The cluster coefficient of node i is defined as $C_i = 2e_i/k_i(k_i-1)$, where k_i is the degree of node i and e_i is the number of links connecting k_i neighbors of node i to one another [26]. When k_i is zero or one, C_i is defined as zero. C_i is equal to one when all neighbors of node i are fully connected to one another, while C_i is zero when none of the neighbors are connected to one another.

Moving stratification by degree. A method of analysis termed moving stratification by degree (MSD) was developed and used to compare three networks, the budding yeast PIN, the human PIN, and a randomly generated network with exactly the same degree distribution as the PINs. Hubs were defined as nodes with degrees of more than six [10,11]. MSD was used to extract sub-networks consisting of hubs with degrees from $k_c-\mu$ to $k_c+\mu$. In this study, we used $\mu = 1$, 3, 5, and 7. Since a hub is defined as a node with degrees of more than 6, we used initial values of $k_c = 7$, 9, 11, and 13. Then, k_c was scanned up to 300 with step size 1. For each initial value ($k_c = 7$, 9, 11, and 13), MSD extracted 293, 291, 289, and 287 sub-networks, respectively. For these sub-networks, only hub nodes were included. In the following analysis, data from $\mu = 5$ were used because changing μ did not significantly alter the results.

The average cluster coefficient $<C(k_c)>$, average shortest path length $<L(k_c)>$, betweeness centrality $B_l(k_c)$, and node ratio included in largest components $G_c(k_c)$ in each sub-network from the PINs were compared with each value from random networks. The sub-networks were tightly connected when the average cluster coefficient was high. While there were no significant differences in the average cluster coefficient between the PINs and random networks for high k_c ($k_c>38$ for the yeast PIN and $k_c>30$ for the human PIN) (Figures S1A and S2A), the average cluster coefficient for PINs was significantly higher than that for the random networks. There were no significant differences in $<L(k_c)>$ and $G_c(k_c)$ between the PINs and random networks (Figures S1B, S1C, S2B, and S2C). It is interesting to note that there were no significant differences in global properties (i.e., betweeness centrality $B_l(k_c)$) between PINs and random networks (see Figures S1D and S2D), although difference in local properties (i.e., average cluster coefficient $<C(k_c)>$) were significant between PINs and random networks (see Figures S1A and S2A).

The fraction of essential proteins to all proteins in each sub-network ($F_{LC}(k_c)$) was investigated for the budding yeast PIN (Figure S1E). The fraction of drug targets to all proteins in each sub-network ($F_{DT}(k_c)$) was investigated for the human PIN (Figure S2E).

There were no known drug-target proteins when k_c was over 50 ($F_{DT}(k_c) = 0$ for $k_c>50$. See Table S4). This means that high-degree proteins were unlikely to be drug targets. However, $F_{DT}(k_c)$ is significantly higher than random expectation when k_c is between 11 and 32. Thus, middle-degree proteins are biologically important and can be drug-target proteins. Table S7 lists middle-degree proteins and their functions categorized by GO annotation. We can expect novel drug targets to be included in the list.

Further analyses were carried out by partitioning a network into three sub-networks, a sub-network consisting of low-degree nodes (degrees from 1 to 5), that consisting of middle-level degree nodes (degrees from 6 to 38 for the yeast PIN and from 6 to 30 for the human PIN), and that consisting of high-degree nodes (degrees more than 39 for the yeast PIN and more than 31 for the human PIN). Middle-level nodes formed a tightly coupled stratus structure whereas high-degree nodes formed a modularized altocumulus structure.

Tables S1 and S2 show that middle-degree nodes formed a high-density tightly coupled structure and a middle-degree sub-network had higher average cluster coefficients than other sub-networks. The average cluster coefficient of PINs without nodes in the middle-degree sub-network was substantially lower than that of the original PIN. In addition, the average shortest distance in the middle-degree sub-network was almost equal to that of the entire PINs. Most nodes in the entire PINs or middle-degree sub-network (over 95% of nodes) were included in the largest component. However, this is not a case for low-degree or high-degree sub-